Transcriptomic analysis of sorted lung cells revealed a proviral activity of the NF-κB pathway towards SARS-CoV-2

Anvita Bhargava[1#], Ugo Szachnowski[2#], Maxime Chazal[1], Dominika Foretek[1,2], Sophie-Marie Aicher[1], Juliana Pipoli da Fonseca[3], Patricia Jeannin[4], Guillaume Beauclair[5], Marc Monot[3], Antonin Morillon[2]*, Nolwenn Jouvenet[1]*

# These authors contributed equally to this work.

* co-corresponding authors

[1] *Institut Pasteur, Université de Paris, CNRS UMR 3569, Virus sensing and signaling Unit, Paris, France*

[2] *CNRS UMR3244, Sorbonne University, PSL University, Institut Curie, Centre de Recherche, Paris, France*

[3] *Institut Pasteur, Université de Paris, Biomics Platform, C2RT, Paris, France*

[4] *Institut Pasteur, Université de Paris, CNRS UMR 3569, Unité Épidémiologie et Physiopathologie des Virus Oncogènes, Paris, France*

[5] *Université Paris-Saclay, CEA, CNRS, Institute for Integrative Biology of the Cell (I2BC), Gif-sur-Yvette, France*

Abstract

Investigations of cellular responses to viral infection are commonly performed on mixed populations of infected and uninfected cells or using single-cell RNA sequencing, leading to inaccurate and low-resolution gene expression interpretations. Here, we performed deep polyA$^+$ transcriptome analyses and novel RNA profiling of SARS-CoV-2 infected lung epithelial cells, sorted based on the expression of the viral spike (S) protein. Infection caused a massive reduction in mRNAs and lncRNAs, including transcripts coding for antiviral factors, such as interferons (IFN). This absence of IFN signaling probably explained the poor transcriptomic response of bystander cells co-cultured with S$^+$ ones. NF-κB pathway and the inflammatory response escaped the global shutoff in S$^+$ cells. Functional investigations revealed the proviral function of the NF-κB pathway and the antiviral activity of CYLD, a negative regulator of the pathway. Thus, our transcriptomic analysis on sorted cells revealed additional genes that modulate SARS-CoV-2 replication in lung cells.

Introduction

Severe acute respiratory syndrome coronavirus 2 (SARS-CoV-2), which emerged in Wuhan, China, at the end of 2019 is the causative agent of Coronavirus Disease-2019 (COVID-19). Infection may be asymptomatic or it may cause a wide spectrum of symptoms, from mild upper respiratory tract infection to life-threatening pneumonia [1]. Viral replication is not limited to the respiratory tract, but rather occurs in numerous organs, including the blood, heart, vessels, intestines, brain and kidneys [2]. Severity of the disease correlates with an excessive pro-inflammatory immune response [3–5], which may be responsible for the symptoms observed in patients. Inflammation is a vital defense mechanism that is required to initiate an adaptive immune response *via* the recruitment and activation of immune cells. However, the non-resolution of acute inflammation leads to tissue damage [6].

SARS-CoV-2 infection is also characterized by a suppression of interferon (IFN) response in infected cells [7]. IFNs are potent antiviral cytokines secreted by various cell types. The IFN response is initiated by the recognition of viral nucleic acids by cellular receptors. Once activated, these receptors recruit adaptor proteins and kinases that trigger the nuclear translocation of the transcription factors IRF3 and NF-κB, which, in turn, induce the rapid expression of IFNs and proinflammatory cytokines [8]. In particular, type I (IFNα and β) and type III (IFN-λ1 and IFN-λ2/3) IFNs play crucial roles in protecting infected and neighboring cells from virus replication and spread. Once secreted, they will signal in a paracrine and autocrine manner through their receptors, activating a signaling cascade that induces the expression of up to 2000 IFN-stimulated genes (ISGs). Their concerted actions establish the antiviral state by targeting specific stages of viral replication [9,10]. SARS-CoV-2 overcomes IFN responses *via* a wide array of mechanisms involving viral proteins [11–13] and a virus-derived microRNA [14,15]. These viral strategies likely contribute to an impaired IFN response in COVID-19 patients [16] and, consequently, high levels of viral replication.

Several transcriptomic analyses of human cells infected with SARS-CoV-2 have been performed to describe the perturbation of cellular pathways induced by infection, using several cellular models, such as human cells derived from lung, bronchial or colorectal tissue [17–19], as well as post-mortem lung samples of COVID-19 patients [17] and bronchoalveolar lavage fluids (BALF) from patients [20]. These genome-wide investigations of host cellular responses to SARS-CoV-2 infection were performed exclusively using bulk RNA-sequencing (RNA-seq) technologies, *i.e.* by analyzing gene perturbations in mixed populations of infected and uninfected cells. Previous studies on Zika virus infected cells have estimated that only 10% of the repressed and about 30% of the induced genes can be identified in a mixed population containing around one third of infected cells [21]. Bulk transcriptome signals are thus partly drawn into noise background, rendering impossible to efficiently and exhaustively portray the full variation of the host transcripts. The perturbation of cellular responses in SARS-CoV-2 infected and bystander cells have also been analyzed using single-cell (sc) RNA-seq methods. Such studies were performed in a variety of cellular models, including COVID-relevant ones, such as human intestinal organoids [22], human tracheal-bronchial epithelial cells [23,24], human lung cell lines [19] and BALF from patients [25]. However, the technical variability, high noise and massive sample size of scRNA-seq data raise challenges in analyzing the total number of differentially expressed genes (DEGs) [26] out of a limited list of only 1000 to 3000 most expressed genes in individual cells. The balance between the number of cells to be sequenced and the sequencing depth to extract the maximum amount of information from the experiment also affects the results [27].

Moreover, most bulk and single-cell transcriptomic studies performed to investigate the cellular response to SARS-CoV-2 focused on the expression of the referenced coding genome, largely ignoring non-coding and unannotated information, mainly represented by long non-coding RNAs (lncRNAs). These RNAs, which are at least 200 nucleotides (nt) in length, are of specific interest since they play fundamental roles in cellular identity, development and disease progression through epigenetic or post-transcriptional regulation of mRNA expression [28]. Combined RNA-seq data from multiple sources reported over 20 000 lncRNA loci in the human genome [29]. Future studies will plausibly increase this number, since lncRNAs are more cell-type specific [30] and expressed at lower levels than mRNAs [29]. Most of them are independently transcribed by RNA polymerase II and, like protein-coding RNAs, they can be 5'-capped, polyadenylated, and spliced by the cellular machinery [31]. Increasing evidence suggests the involvement of lncRNAs in virus-host interactions and antiviral immunity [32–34]. Current efforts focus on uncovering unannotated RNAs, which could encompass a variety of RNA biotypes, from rare mRNA isoforms to unannotated intergenic long noncoding RNAs, using reference-based approach with the human gencode annotation [35]. However, so far, none of these strategies have been engaged to dissect virus-cell interactions.

Here, we investigated the coding and non-coding transcriptional landscape of lung cells infected with SARS-CoV-2, sorted according to the expression of the viral protein spike (S). Our deep transcriptome analysis using annotated RNA genes and reference-based RNA profiler uncovered

100 pathways that are directly affected by infection and identified coding and non-coding genes contributing
101 to an optimal SARS-CoV-2 replication.
102
103
104 **Results**
105 **Transcriptional landscapes of SARS-CoV-2-infected and bystander lung cells uncovered a global**
106 **expression shutoff**
107 To analyze transcriptomic changes in infected and bystander cells, human alveolar basal epithelial
108 carcinoma cells (A549) stably expressing the viral receptor ACE2 (A549-ACE2) were infected with a
109 MOI of 1 for 24 hours, fixed, stained intracellularly using antibodies against S proteins and sorted into
110 S-positive (infected cells, S^+) and S-negative (bystander, S^-) populations (Fig. 1A and 1B). Around 15%
111 of A549-ACE2 cells were positive for S protein (Fig. 1B). Cells negative for S protein represent either
112 uninfected cells or cells at an early stage of infection, prior to viral protein production. Mock-infected
113 cells served as negative controls. The experiment was performed twice independently in triplicates.
114 PolyA+ RNAs were isolated from mock-infected, S^+ and S^- cells. Around 85% of the total reads mapped
115 to the viral genome in S^+ cells, while less than 5% of the total reads aligned with the viral genome in S^-
116 cells (Fig. 1C), validating our sorting approach. The large dominance of viral reads over cellular reads
117 illustrates the ability of the virus to hijack the cellular machinery for its replication. A similar proportion
118 of SARS-CoV-2 reads in the RNA pool was previously reported in lung epithelial carcinoma Calu-3
119 cells infected for 8 hours [18]. These differences in the representation of viral RNA between S^+ and S^-
120 cells altered the robustness of the statistical analysis used to identify DEGs. To overcome this limitation,
121 the samples were depleted of viral RNAs (vRNAs) using a set of oligonucleotide probes covering the
122 entire viral genome (Fig. 1A). Following depletion, viral reads represented between 0,01 and 2,8% of
123 the total reads both in S^+ and S^- cells (Fig. 1C).
124 Coding and long non-coding genes were identified using gencode annotation (v32), while
125 unannotated RNAs were recovered with Scallop assembler [35] (Fig. 1D-F, Fig. S1A-B and tables S1-
126 S3). Principal component analysis (PCA) of polyA+ transcriptomes segregated S^+ cells from S^- and
127 mock-infected ones (Fig. 1D). This segregation based on S expression represented around 92% of the
128 transcriptomic differences between the samples (Fig. 1D). Only subtle differences (2,5%) distinguished
129 bystander and mock-infected cells (Fig. 1D), suggesting that the transcriptional landscapes of these 2
130 cell populations were very similar. An absence of response of S^- cells was unexpected since cytokines,
131 which are commonly secreted by virally infected cells, activate an antiviral state in bystander cells
132 through surface receptors.
133 Analysis of gene expression allowed identification of thousands of annotated coding and non-
134 coding genes that were differentially expressed (absolute fold change ≥ 2, p-value < 0.05) in S^+ cells as
135 compared to S^- or mock-infected ones (Fig. 1E-F and tables S1-S3). We identified around 13 times more
136 downregulated coding genes than upregulated ones in S^+ cells (Fig. 1E-F), suggesting that infection

137 triggers a massive, but incomplete, shutoff of gene expression and/or degradation of host RNAs. Among
138 the top upregulated coding genes in S^+ cells, we confirmed candidates revealed by previous analyses
139 performed in non-sorted non-vRNA-depleted A549-ACE2 cells, such as CXCL8, CCL20, IL6 and
140 NFKB1 [17,36,37], but also novel highly significant candidates, including IL32 and ITGAM (table S1).
141 The genes encoding IFN type I and type III were not upregulated in S^+ cells, as compared to mock-
142 infected cells (Fig. S1C). Accordingly, ISGs were not upregulated either in S^+ cells. This absence of
143 innate immune response in infected cells agrees with previous analyses performed in mixed population
144 of A549-ACE2 cells infected with SARS-CoV-2 [17,36,37]. Such absence of innate response reflects
145 the ability of the virus to potently inhibit the IFN response *via* numerous mechanisms in human cells
146 [12]. Around 1260 annotated lncRNAs were downregulated in S^+ cells as compared to mock-infected
147 cells, and 184 were upregulated (Fig. 1E-F and table S2). RFPL3S, ADIRF-AS1 and WAKMAR2 were
148 among the top 15 upregulated lncRNAs in S^+ cells. RFPL3S and ADIRF-AS1 have no known functions,
149 whereas WAKMAR2 restricts NF-kB-induced production of inflammatory chemokines in human
150 keratinocytes [38]. Among the top downregulated lncRNAs, we identified HOXA-AS2 and NKILA,
151 which are negative regulators of NF-kB signaling, in endothelial cells and breast cancer cell lines,
152 respectively [39,40]. Altered expression of WAKMAR2, HOXA-AS2 and NKILA in infected cells
153 could thus play a role in viral-associated inflammation. From the 1400 unannotated transcripts we
154 detected using Scallop assembler [35], around 800 unannotated polyA+ transcripts were also
155 differentially expressed in S+ cells as compared to S^- ones (Fig. 1E-F and table S3).
156 In agreement with the PCA (Fig. 1D), volcano plots and heat maps revealed that S^- bystander cells
157 and mock-infected control cells exhibited very similar transcriptomic profiles (Fig. 1E-1F and Fig. S1A-
158 S1B). Only around 170 polyA+ transcripts were differentially expressed in S^- cells as compared to
159 mock-infected ones (Fig. 1E and tables S1-S3). As a comparison, over 13000 DEGs were identified in
160 S^+ as compared to mock-infected cells (Fig. 1E and tables S1-S3). These analyses further suggest that
161 S+ cells present none or very little paracrine signaling response. Among the 69 coding genes that were
162 upregulated in S^- cells as compared to mock-infected, 29 were also upregulated in S^+ cells (Fig. S1B
163 and table S3). Some of these common genes were inflammatory genes, such as IL32, IL6 and CCL20.
164 Among the 39 upregulated coding genes that were unique to S^- cells, 16 were ISGs (examples include
165 MX1, APOL1 and IFI6). The expression of these inflammatory genes and ISGs in bystander cells could
166 be induced early in infection, prior to the production of S protein.
167 Our approach reveals that SARS-CoV-2 infection triggers a major down-regulation of gene
168 expression in A549-ACE2 cells. It also shows that S^- cells do not exhibit a strong transcriptional
169 signature despite being cultured with S^+ cells, suggesting the absence of an efficient paracrine
170 communication.
171
172 **Separating lung cells based on the expression of the viral S protein improved discovery of DEGs**

173 To compare our differential deep analyses with known datasets, we analyze publicly available
174 polyA+ RNA-seq raw data of unsorted A549-ACE2 infected with SARS-CoV-2 at a MOI of 0.2 [17].
175 Viral reads represented around 50% of the total number of reads in these unsorted bulk population of
176 cells [17], which was expectedly less than in A549-ACE2 cells positive for S (Fig. 1C). The 2 analyses
177 shared 150 upregulated protein-coding genes and 238 downregulated ones (Fig. 2A, table S4). The vast
178 majority (about 80%) of the downregulated mRNAs that we identified were classified as 'unchanged'
179 in the analysis of unsorted cells (Fig. 2A, table S4). Thus, sorting cells based on S expression and
180 depleting viral RNA allowed the identification of over 30 times more downregulated coding genes than
181 in unsorted cells (Fig. 2A, table S4). The poor sensibility of analysis of mixed cell population in
182 detecting downregulated genes is likely due to the large proportion of non-infected cells, in which the
183 majority of genes remained normally expressed, thus masking any decrease of gene expression in the
184 pool of infected cells. Indeed, an artificial reconstruction of a mixed cell population (80% S^- and 20%
185 S^+) supports this hypothesis (Fig. S2). About 41% of the upregulated protein-coding genes and 16% of
186 downregulated ones that we identified were not detected in conventional RNA-seq analysis of mixed
187 populations [17]. This comparison highlights the accuracy and the depth of our analysis.
188 To validate the sorting approach combined with vRNA-depletion, we compared mRNA
189 abundances of a few DEGs in a bulk population of cells infected with SARS-CoV-2 for 24 hours, as
190 well as in sorted S^+ and bystander S^- cells infected in the same condition. As expected, S+ cells produced
191 approximately 200-fold more intracellular viral RNAs than did S^- cells (Fig. 2B). These qPCR analyses
192 confirm that some S^- cells are at an early stage of viral replication, prior to viral protein expression (Fig.
193 1B). We included in the analysis three coding transcripts (IL32, ITGAM and TRAF1), two lncRNAs
194 (WAKMAR2 and AL132990.1) and one unannotated transcript (XLOC_007519) that were identified
195 amongst the most upregulated RNAs in S^+ A549-ACE2 cells (Fig. 2C, S3A, S3B and tables S1-S3). The
196 abundance of IL32 mRNA did not increase significantly in the infected bulk population, as compared
197 to mock-infected cells (Fig. 2C). By contrast, IL32 mRNA levels increased around 30-fold in S^+ cells,
198 compared to those in mock-infected cells (Fig. 2C). This difference explains why IL32 was not identified
199 as an up-regulated gene in previous RNA-seq analysis performed in mixed population of infected A549-
200 ACE2 cells [17,36]. Similarly, the expression of ITGAM, TRAF1, WAKMAR2, AL132990.1 and
201 XLOC_007519 showed a modest increase in the bulk population and a significant increase in S^+ cells,
202 as compared to mock-infected cells (Fig. 2C and S3B). The decreased expression of transcripts
203 identified as top downregulated hits in the RNA-seq analysis of S+ cells, such as the coding transcripts
204 FEN1 and SNRPF, the lncRNAs AC016747.1, DANCR and TP53TG1, as well as the unannotated RNA
205 XLOC_049236 (Fig. 2D, S3A and S3C), was significantly more pronounced in S^+ cells than in the
206 mixed population of cells, when compared to mock-infected cells (Fig. 2D and S3C). Analysis of RNA
207 abundances in sorted cells thus highlighted the increased accuracy of our approach, compared to
208 classical methods, in detecting up- and down- regulated genes.

209 To identify pathways affected by infection in A549-ACE2 cells, we performed Gene Ontology
210 (GO) terms and KEGG pathway enrichment analysis on the upregulated coding genes in S^+ cells, as
211 compared to mock-infected cells (Fig. 2E). We observed a significant enrichment in several
212 inflammatory signaling pathways, including TNF and NF-κB signatures, which were previously
213 identified in bulk transcriptomic analysis of infected A549 and Calu-3 cells [36,37] and in scRNA-seq
214 analysis of infected colon and ileum organoids [22]. Members of the superfamily of TNF proteins are
215 multifunctional proinflammatory cytokines. NF-κB plays an important role in promoting inflammation,
216 as well as regulating cell proliferation and survival [41]. Activation of NF-κB is one of the signals
217 transduced by the TNF-superfamily members [42]. These inflammatory signatures are also consistent
218 with those observed in peripheral blood immune cells of severe or critical COVID-19 patients [16].
219
220 **Inflammatory cytokines, but not IFNs, are produced and secreted by infected cells.**
221 We wondered whether the underwhelming response of the bystander S^- cell population could be
222 explained by a defect in paracrine communication between S^+ and S^- cells. Despite being present in high
223 abundance in S^+ cells as compared to mock-infected cells (table S1 and Fig. 2E), inflammatory cytokine
224 transcripts may not be translated. Indeed, initiation of translation seems to be impaired in SARS-CoV-
225 2 infected cells via two potential mechanisms: acceleration of cytosolic cellular mRNA degradation [18]
226 and blockade of the mRNA entry channel of ribosomes by the viral protein Nsp1 [43–45]. Moreover,
227 viral proteins Nsp8 and Nsp9 disrupt protein secretion in HEK293T cells [43], raising the possibility
228 that cytokines are produced but not secreted by S^+ cells.
229 To investigate these possibilities, we selected 5 inflammatory chemokines (IL-6, CXCL1, CCL2,
230 CXCL8/IL-8 and CCL20) whose expression was upregulated in S^+ cells upon infection (table S1) and
231 quantified their intracellular and secreted levels in lysates and supernatants of A549-ACE2 cells infected
232 for 24 hours (Fig. 3A-B). For comparison, A549-ACE2 cells transfected with the immuno-stimulant
233 poly(I:C) were included in the analysis. In a mixed population of S^+ and S^- cells, mRNAs of these 5
234 cytokines were significantly more abundant than in mock-infected cells (Fig. S4A), in agreement with
235 the increased levels of mRNAs detected in S^+ cells by RNA-seq (table S1). Their expression was also
236 induced by poly(I:C) (Fig. S4A). All five cytokines were expressed at detectable levels in cells
237 stimulated by viral infection or poly(I:C) (Fig. 3A), indicating that infection does not hamper the
238 translation of the corresponding mRNAs. As expected, based on their mRNA abundance (Fig. S3A),
239 intracellular levels of IL-6, CCL2 and IL-8 significantly increased upon poly(I:C) stimulation as
240 compared to unstimulated control cells (Fig. 3A). By contrast, despite being induced by poly(I:C)
241 downstream signaling (Fig. S4A), CXCL1 and CCL20 levels were comparable in stimulated and
242 unstimulated cells (Fig. 3A). This could be due to a short protein half-life, protein degradation and/or
243 rapid secretion. Intracellular levels of CXCL1 increased significantly upon infection compared to mock-
244 infected cells (Fig. 3A) while intracellular levels of IL-6, CCL2, IL-8 and CCL20 were similar in both
245 conditions. However, all 5 cytokines were significantly more secreted by infected cells than mock-

246 infected ones (Fig. 3B). Infected cells secreted even more IL-6 and CXCL1 than cells stimulated by
247 poly(I:C) (Fig. 3B). Thus, inflammatory cytokines are expressed and secreted by A549-ACE2 cells
248 infected with SARS-CoV-2, which is in line with the excessive inflammatory response reported in other
249 cellular models [17,19,22,24,37] and characteristic of severe cases of COVID-19 [3–5]. The absence of
250 paracrine communication that was revealed by the RNA-seq analysis of S^- cells (Fig. 1) is thus unlikely
251 to be linked to a defect in cytokine expression and secretion in S^+ cells. It may be explained by the
252 apparent absence of IFN signaling. Indeed, and consistently with prior RNA-seq studies conducted in
253 bulk A549-ACE2 cells [17,36,37], we failed to observe a significant IFN- signature in S^+ cells (table
254 S1, Fig. 2E and Fig. S1D), despite a robust induction of NF-κB activity (Fig. 2E).
255 To validate this further, we compared the level of IFNβ, IFN-λ1 and IFN-λ2/3 transcripts in
256 A549-ACE2 cells infected for 24 hours. Cells treated with poly(I:C) were used as positive controls for
257 IFN production. Cells infected with Measles virus (MeV), a respiratory RNA virus known to trigger an
258 IFN response in A549 cells [46], were also included in the analysis for comparison. Flow cytometry
259 analysis identified on average 20 to 30% of cells positive for viral proteins upon SARS-CoV-2 or MeV
260 infection (Fig. 3C). As expected, the level of IFNβ, IFN-λ1 and IFN-λ2/3 transcripts increased in
261 poly(I:C)-treated cells compared to cells exposed to the transfecting reagent lipofectamine only (Fig.
262 S3B). Amounts of IFNβ, IFN-λ1 and IFN-λ2/3 transcripts were several orders of magnitude higher in
263 MeV-infected cells than in SARS-CoV-2 infected cells (Fig. S4B). Consistently with mRNA level
264 analysis (Fig. S4B), around 200 and 850 pg/ml of IFNβ were secreted by MeV-infected cells and
265 poly(I:C)-treated cells, respectively (Fig. 3D). SARS-CoV-2 infected cells secreted as little as 50 pg/ml
266 of IFNβ, which was similar to the quantity secreted by mock-infected cells and lipofectamine-exposed
267 cells, likely representing baseline levels (Fig. 3D). MeV infected cells secreted around 1000 pg/ml of
268 IFN-λ1 and 5000 pg/ml of IFN-λ2/3 while no IFN-λ was detected in the supernatant of SARS-CoV-2
269 infected cells (Fig. 3D). This baseline level of IFN type-I secretion and absence of IFN type-III release
270 by SARS-CoV-2-infected cells is likely to be responsible for the lack of paracrine signaling revealed by
271 the RNA-seq analysis (Fig. 1). These analyses indicates that inflammatory cytokines, but not IFNs, are
272 produced and secreted by infected cells.
273
274 **Coding and non-coding NF-κB targets escaped the virus-induced cellular shutoff**
275 Numerous genes associated with the NF-κB signaling pathway fall into the category of genes that
276 escaped the virus-induced cellular shutoff (Fig. 2E). To determine which of these genes were directly
277 controlled by NF-κB, we cross-compared the upregulated genes with known NF-κB target genes.
278 Among the 68 upregulated NF-κB-targets in S^+ cells, we identified cytokines such as CXCL8/IL8 and
279 IL32 (Fig. 4A, S5A and table S5). NFKB1, which codes for the p105/p50 subunit of the transcription
280 factor, and is itself a NF-κB-target gene [47,48], also showed a significant transcriptional induction in
281 S^+cells (Fig. 4A and S5A), as well as in a bulk population of infected cells (Fig. S5B). Such mechanism
282 generates an auto-regulatory feedback loop in the NF-κB response [47].

283 To identify NF-κB-driven lncRNAs, we analyzed NF-κB chromatin immunoprecipitation (ChIP)-
284 sequencing data generated in A549 cells stimulated with TNFα [49] and searched for known NF-κB
285 binding motifs [103]. The analysis recovered 15 NF-κB-targets among the 184 upregulated lncRNAs in
286 S^+ cells (Fig 4A and table S5), including PACERR, which is known to modulates the expression of NF-
287 κB-target genes *via* a direct interaction with the p50 subunit in U937 macrophages [50]. Novel NF-κB
288 target genes were also identified among unannotated genes (Fig 4A and table S5).
289 To determine whether the lncRNAs identified by the *in silico* analysis were indeed NF-κB targets,
290 RT-qPCR analysis were performed to assess the levels of three lncRNAs (CYLD-AS1, lnc-RASSF5
291 and lnc-HS3ST3B1-1:2) following 3 hours of TNFα treatment, and, as a comparison, after 24 hours of
292 SARS-CoV-2 infection (Fig. S6). IL6, CXCL8 and CCL20 were included as positive controls for NF-
293 κB activation. As expected, both TNFα treatment and SARS-CoV-2 infection significantly increased
294 the levels of IL6, CXCL8 and CCL20 mRNAs, as compared to non-treated cells (Fig. S6A). The
295 transcription of CYLD-AS1, lnc-RASSF5 and lnc-HS3ST3B1-1:2 was also induced in TNFα-treated
296 cells (Fig. S6B), as well as in SARS-CoV-2 infected cells, albeit not significantly for lnc-RASSF5 (Fig.
297 S6B). This suggests that transcription of these three lncRNAs occurs via activation of the NF-κB
298 pathway. To confirm that the NF-κB subunit p65 directly binds the upstream promoter of the lncRNAs
299 of interest, a Cut & Run assay was performed to identify direct p65 targets upon TNFα stimulation in
300 A549-ACE2 cells (Fig. 4B). Sequencing results confirmed the presence of direct p65 docking upstream
301 of transcription starts sites (TSS) of the 15 NF-κB-driven lncRNAs identified *in-silico*, except ADIRF-
302 AS1 (Fig. 4B). Thus, coding and non-coding NF-κB targets escaped the virus-induced cellular shutoff.
303
304 **The NF-κB signaling pathway is required for an optimal SARS-CoV-2 replication**
305 For functional analysis, we selected NFKB1, CXCL8/IL8 and IL32, which were among the top
306 upregulated NF-κB target genes identified in S^+ cells (Fig. 4A). NFKB1 served as a positive control in
307 these experiments since reducing its expression was previously shown to decrease SARS-CoV-2 protein
308 expression in A549-ACE2 cells [36]. These results were initially unexpected since NF-κB commonly
309 acts as antiviral factor [41]. Analysis of mRNA abundances showed a significant transcriptional
310 induction of NFKB1 and CXCL8/IL8 in a bulk population of A549-ACE2 cells infected by SARS-CoV-
311 2 for 24 hours, as compared to mock-infected cells (Fig. S5B), validating the RNA-seq analysis
312 performed on S^+ cells (Fig. 1). We had previously confirmed that IL32 transcripts were significantly
313 more abundant in S^+ cells than in mock-infected cells (Fig. 2C). We explored the potential ability of
314 NFKB1, CXCL8 and IL32 to modulate the replication of SARS-CoV-2 using siRNA-mediated knock-
315 down approaches. siRNA pools efficiently reduced the expression of their respective targets in A549-
316 ACE2 cells (Fig. 4C). Reduced expression of NFKB1, CXCL8 and IL32 significantly decreased
317 intracellular viral RNA yield twenty-four hours post-infection (Fig. 4D). The number of cells positive
318 for the viral protein S, as well as infectious viral particle production, were also significantly reduced in

319 cells expressing low levels of NFKB1, CXCL8 and IL32, as compared to cells transfected with control
320 siRNA pools (Fig. 4E-F). These results confirmed the pro-SARS-CoV-2 activity of NFKB1 in A459-
321 ACE2 cells [36] and revealed that CXCL8 and IL32 also exhibited significant proviral functions. Thus,
322 our sorting approaches identified upregulated NF-κB target genes that contribute to an optimal SARS-
323 CoV-2 replication.
324
325 **CYLD reduced SARS-CoV-2 infection by dampening inflammation**
326 CYLD-AS1 is one of the NF-κB dependent lncRNAs induced by SARS-CoV-2 infection that was
327 detected via the *in silico* approach and validated by the Cut & Run analysis (Fig. 5A) It caught our
328 attention since it arises from the strand opposite to the protein-coding gene CYLD, which is also
329 upregulated by SARS-CoV-2 infection (Table S1). CYLD-AS1 and CYLD share the same promoter for
330 bidirectional transcription, within which we detected a peak for direct p65 binding (Fig. 5A). CYLD has
331 deubiquitinating activity and negatively regulates the NF-κB pathway, thus limiting persistent
332 inflammation [51]. It does so by removing poly-ubiquitin tails from upstream signaling factors such as
333 TRAF2 and TRAF6, thus terminating signal transduction [51]. To investigate the role of CYLD in
334 SARS-CoV-2 infection, we used siRNAs to knock-down its expression prior to infection. Knockdown
335 efficiency was confirmed at the transcript and protein levels (Fig. 5B-C). Consistent with our RNA-Seq
336 data, infection increased the abundance of CYLD, leading to a partial rescue of CYLD transcript levels
337 after siRNA treatment (Fig. 5B). The proportion of S^+ cells was significantly higher in cells expressing
338 reduced levels of CYLD compared to control cells (Fig. 5D). As expected based on its known function
339 [51], depletion of CYLD led to increased expression levels of the mRNAs of the inflammatory cytokines
340 IL-6, CCL2 and IL-8 /CXCL8 upon infection (Fig. 5E). In agreement with this, less IL-6, CCL2 and IL-
341 8 were secreted in unstimulated cells expressing reduced levels of CYLD compared to control cells (Fig.
342 5F). These results suggest that CYLD acts as an antiviral factor for SARS-CoV-2, most likely by
343 negatively regulating the proviral NF-κB pathway (Fig. 5G).
344
345 **Discussion**
346 Transcriptomic analysis of lung A549-ACE2 cells sorted based on Spike expression permitted deep
347 sequencing of many cells synchronized for viral protein expression. Depletion of viral RNA from the
348 samples prior to RNA-seq allowed for a robust identification of host cell DEGs. Our approach thus
349 unveiled an accurate and comprehensive picture of genome-wide signaling networks that are directly
350 affected by SARS-CoV-2 replication in human lung cells. It revealed a massive, but somehow selective,
351 gene expression shutoff in S^+ cells. Such reduction of cellular transcripts was underestimated in analysis
352 performed on bulk population of infected A549-ACE2 cells [17,36,37] but was detected by RNA-seq
353 analysis performed on bulk population of Calu-3 cells infected at an high MOI [18]. This is probably
354 due to the fact that Calu-3 cells express high levels of ACE2 [52] and are thus naturally permissive to
355 SARS-CoV-2, ensuring a high proportion of infected cells in the mixed culture. SARS-CoV-2 employs

356 several strategies to decrease the level of cellular mRNAs in infected cells, including inhibition of
357 nuclear mRNA export [18,43] and accelerated mRNA degradation as compared to control cells [18].
358 SARS-CoV-1 and SARS-CoV-2 Nsp1 largely contribute to these processes by interacting with the
359 mRNA export machinery [53] and by inducing endonucleolytic cleavage of the 5′ UTR of capped
360 mRNAs bound to 40S ribosomes [18,54–56]. SARS-CoV-2 RNAs are protected from Nsp1-mediated
361 degradation by their 5' end leader sequence [18,57], which explains why we observed, in agreement
362 with previous studies performed in A549-ACE2 cells [17] and Calu-3 cells [18], a large dominance of
363 viral RNA over the cellular RNA pool at 24 hpi.

364 One consequence of this drastic shutoff is the suppression of induction of innate immune genes,
365 such as IFN type I and type III. In agreement with previous RNA-seq studies performed in bulk
366 populations of infected A549-ACE2 cells [17,36] and kidney HEK293T-ACE2 cells [58], our
367 transcriptomic profiling combined with analysis of mRNA levels and IFN secretion showed that infected
368 cells failed to mount an antiviral response. Besides global gene expression reduction in host cells, SARS-
369 CoV-2 has evolved numerous mechanisms to specifically counteract the IFN induction and signaling
370 pathways [12]. For instance, the viral proteins Nsp6 and Nsp13 bind and block the ability of TANK
371 binding kinase 1 (TBK1) to phosphorylate IRF3 [11] and several viral proteins, including the N and
372 Orf6 proteins, dampen STAT1/2 phosphorylation or nuclear translocation [11,59,60]. Consistent with
373 an absence of IFN secretion by S^+ cells and, consequently, a poor paracrine response, the transcriptome
374 of bystander S^- cells largely overlapped with the one of mock-infected cells.

375 Absence of IFN response is not, however, a universal feature of SARS-CoV-2 infection. Viral
376 replication induces a type I and III IFN response in Calu-3 cells [61–64], primary airway epithelia
377 cultured at the air-liquid interface [61,63], human intestinal epithelial cells [65], organoid-derived
378 bronchioalveolar models [66] and intestinal organoids [67]. When infected at a high MOI, A549-ACE2
379 cells also induced expression of IFN and ISGs [17]. Thus, *in vitro*, the magnitude of the IFN response
380 elicited by SARS-CoV-2 is cell-type specific and dependent on the viral load. Nevertheless, RNA-seq
381 analysis of postmortem lung tissues from lethal cases of COVID-19 failed to detect IFN-I or IFN-III
382 [17]. Type I IFN responses were highly impaired in peripheral white blood cells of patients with severe
383 or critical COVID-19, as indicated by transcriptional analysis [16]. Moreover, infected patients had no
384 detectable circulating IFN-β, independently of the severity of the disease [16]. Thus, our results
385 corroborate these clinical studies highlighting the efficient shutdown of IFN production by the virus.

386 Although our RNA-seq analysis identified over 12000 host transcripts that were significantly
387 reduced during SARS-CoV-2 infection as compared to control cells, it also recovered around 1500
388 transcripts whose levels were significantly elevated and 2800 transcripts whose levels were unchanged
389 upon infection. Among top upregulated genes in S^+ cells, we identified numerous proinflammatory
390 cytokines, such as IL6, CXCL1, CCL2, IL8/CXCL8 and CCL20. ELISA analysis confirmed that
391 infected cells were producing these inflammatory cytokines. They were previously identified in bulk or
392 sc-RNAseq analysis of A549-ACE2 cells as upregulated [17,36,37], while others, such as IL32, were

393 underreported. High levels of proinflammatory cytokine transcripts have been also observed in infected
394 primary bronchial cells [17], lung macrophages [25] and post-mortem lung samples of COVID-19-
395 positive patients [17]. Thus, SARS-CoV-2 appears to selectively inhibit IFN signaling while allowing
396 chemokine production in lung cells.

397 GO and KEGG pathway analyses confirmed the upregulation of an inflammatory response in S^+
398 cells, including TNF- and NF-κB- transcriptional signatures. An NF-κB transcriptional footprint was
399 previously identified in RNA-seq analysis of bulk population of SARS-CoV-2-infected tracheal-
400 bronchial epithelial cells [24] and in scRNA-seq analysis of infected A549-ACE2 cells [36]. Microarray
401 analysis of Calu-3 cells infected with SARS-CoV-2 also showed a specific bias towards an NF-κB
402 mediated inflammatory response [37]. Finally, inflammatory genes specifically up-regulated in
403 peripheral blood immune cells of severe patients or critical COVID-19 patients mainly belonged to the
404 NF-κB pathway [16]. Consistently, among the 741 upregulated protein-coding genes that we identified
405 in S^+ cells, 68 possess an NF-κB binding site in their promoter regions. Examples include IL6,
406 CXCL8/IL8 and IL32. We also identified NF-κB binding site in the promoter regions of lncRNAs that
407 were upregulated in S^+ cells, such as CYLD-AS1 and PACERR, both by *in silico* and Cut-and-Run
408 analysis. NF-κB contribution to the antiviral response is well described and is supported by numerous
409 *in vivo* experiments showing that mice deficient in different NF-κB subunits are more susceptible to
410 viral infection than wild-type mice [41]. Consistently, many viruses have evolved strategies to
411 counteract the NF-κB-mediated antiviral response [68]. However, certain human viruses, such as HIV-
412 1, Epstein-Barr virus and influenza A virus, activate NF-κB to block apoptosis and prolong survival of
413 the host cell to gain time for replication [69]. Our data show that disruption of NF-κB function through
414 silencing of its subunit p105/p50 diminished the production of viral RNAs and proteins at 24 hpi in
415 A549-ACE2 cells, confirming its proviral role [36,37]. Several SARS-CoV-2 proteins could contribute
416 to the activation of NF-κB signaling in infected cells. When individually expressed, Orf7a and Nsp14
417 activate NF-κB signaling pathway and induce cytokine expression, in Hela and HEK293T cells,
418 respectively [70,71]. Nsp5 also induces the expression of several inflammatory cytokines, such as IL-6
419 and TNF-α, through activation of NF-κB in Calu-3 and THP1 cells [72]. Further studies are required to
420 understand how SARS-CoV-2 benefits from hijacking NF-κB-driven functions.

421 Consistent with a proviral role of NF-κB in the context of SARS-CoV-2 infection, we found that
422 diminished expression of two NF-κB target genes (IL32 and CXCL8/IL8,) significantly decreased viral
423 RNA, viral protein production and infectious viral titers. IL-32 is a proinflammatory interleukin secreted
424 by immune and non-immune cells that induces the expression of other inflammatory cytokines,
425 including TNF-α, IL-6, and IL1β [73]. IL-32 was previously described as an antiviral factor in the
426 context of infection with several RNA and DNA viruses. For instance, its secretory isoform reduces the
427 replication of Hepatitis B virus by stimulating the expression of IFN-λ1 [74]. Its antiviral activity was
428 also demonstrated in U1 macrophages infected with HIV-1 [75] and canine kidney cells infected with
429 influenza A [76], using silencing and over-expression approaches, respectively. Further studies are

430 required to understand the pro-SARS-CoV-2 function of endogenous IL-32. It may support SARS-CoV-
431 2 replication *via* its ability to activate NF-κB [77]. IL-8 is a potent neutrophil chemotactic factor. It was
432 previously shown to possess proviral functions in the context of infection by several unrelated RNA and
433 DNA viruses, probably via inhibition of the antiviral action of IFN-α [78,79]. It could act in a similar
434 manner in SARS-CoV-2 infected A549-ACE2 cells. CYLD, which is an upregulated gene in S+ cells,
435 is a negative regulator of the NF-κB pathway [51] but its role in SARS-CoV-2 has not been documented
436 so far. Our data suggest that it acts as an antiviral factor, further confirming the proviral role of NF-κB
437 in the context of SARS-CoV-2 infection.

438 As for coding genes, there was a higher proportion of down- *versus* up-regulated lncRNAs in S^+
439 cells. GO cannot be extrapolated from lncRNAs since most of them have no known function, indicating
440 the need for future studies in this area. Several RNA-seq and microarray studies have identified hundreds
441 of lncRNAs induced by IFN stimulation or viral infection in diverse human and mice cell types
442 [33,34,80–82]. Analysis of a handful of them has provided a glimpse of the potential regulatory impact
443 of this class of RNAs on the IFN response itself [83] and on ISG expression [33,80,82]. However, the
444 investigation of the precise role of individual lncRNAs in IFN-mediated antiviral response is still in its
445 infancy stage. By analyzing publicly available SARS-CoV-2-infected transcriptome data, several
446 studies recovered lncRNAs that were misregulated upon infection of human lung epithelial cell lines,
447 primary normal human bronchial epithelial cells and BALF [84–87]. However, no lncRNA with a direct
448 action on the life cycle of SARS-CoV-2 has been identified yet.

449 Finally, our analysis profiled about 600 differentially expressed unannotated polyA+ transcripts in
450 S+ and bystander cells. The identification of these unannotated genes confirms that the human genome
451 is far from being well characterized. Having specific RNAs expressed in particular conditions could
452 open the way for the identification of pro- or anti-viral genes that could be used for better prognosis of
453 at-risk patients or for the follow up of the disease severity.

454 Our data suggests that the genes that are refractory to the viral-induced shutoff are mostly proviral
455 genes. Understanding the molecular mechanisms underlying the selectivity of the shut-off would be
456 interesting. Since coronavirus Nsp1 induces the cleavage of the 5'UTR of capped transcripts bound to
457 40S ribosomes, the 5'UTR length and/or structure may affect Nsp1 binding and subsequent degradation.
458 Alternatively, the extent of transcript reduction may be linked to their GC content and/or their lengths,
459 which could affect the specificity of the host RNase that is presumably recruited by Nsp1. Discovering
460 the host RNase responsible for transcript degradation in SARS-CoV-2-infected cells will shed light on
461 the mechanism of selectivity of the viral-induced shutoff.

462

463 **Material and Methods**

464 **Cell lines.** Human lung epithelial A549-ACE2 cells, which have been modified to stably express
465 ACE2 *via* lentiviral transduction, were generated in the laboratory of Pr. Olivier Schwartz (Institut
466 Pasteur, Paris, France). A549-ACE2 and African green monkey Vero E6 cells (ATCC CRL-1586) were

467 cultured in high-glucose DMEM media (Gibco), supplemented with 10% fetal bovine serum (FBS;
468 Sigma) and 1% penicillin-streptomycin (P/S; Gibco). Cells were maintained at 37°C in a humidified
469 atmosphere with 5% CO_2.

470 **Virus and infections.** Experiments with SARS-CoV-2 isolates were performed in a BSL-3
471 laboratory, following safety and security protocols approved by the risk prevention service of Institut
472 Pasteur. The strain BetaCoV/France/IDF0372/2020 was supplied by the National Reference Centre for
473 Respiratory Viruses hosted by Institut Pasteur (Paris, France) and headed by Pr. S. van Der Werf. The
474 human sample from which the strain was isolated has been provided by Dr. X. Lescure and Pr. Y.
475 Yazdanpanah from the Bichat Hospital, Paris, France. Viral stocks were produced by amplification on
476 Vero E6 cells, for 72 h in DMEM 2% FBS. The cleared supernatant was stored at 80°C and titrated on
477 Vero E6 cells by using standard plaque assays to measure plaque-forming units per ml (PFU/ml). A549-
478 ACE2 were infected at MOI of 1 in DMEM without FBS. After 2 h, DMEM with 5% FBS was added
479 to the cells. The Measles Schwarz strain expressing GFP (MeV-GFP) was described previously [88]
480 and was used at an MOI of 1.

481 **Poly I:C and TNF-α stimulation.** Cells were stimulated with 10 ng/µL Poly(I:C) (HMW, #vac-
482 pic Invivogen) using Lipofectamine 3000 Reagent (Thermo Fisher Scientific) according to
483 manufacturer's protocol. Treatment was maintained for 24 hours, concomitantly with infection.
484 Recombinant human TNF-α (R&D Systems 210-TA/CF) was added directly to cell culture medium at
485 a final concentration of 10 ng/mL and maintained for 3 or 24 hours as indicated.

486 **Flow cytometry.** Cells were detached with trypsin, washed with PBS and fixed in 4% PFA for 30
487 min at 4°C. Intracellular staining was performed in PBS, 2% BSA, 2mM EDTA and 0.1% Saponin
488 (FACS buffer). Cells were incubated with antibodies recognizing the spike protein of SARS-CoV-2
489 (anti-S2 H2 162, a kind gift from Dr. Hugo Mouquet, Institut Pasteur, Paris, France) and subsequently
490 with secondary anti-human AlexaFluor-647 antibody (1:1000, A21455 Thermo) for 30 min at 4°C. Data
491 were acquired using Attune NxT Acoustic Focusing Cytometer (Thermo Fisher) and analyzed using
492 FlowJo software.

493 **Western Blotting.** Cells were lysed in radioimmunoprecipitation assay (RIPA) buffer (Sigma-
494 Aldrich) supplemented with a protease and phosphatase inhibitor cocktail (Roche) for 15 minutes at 4
495 °C under agitation. Supernatants were recovered and samples were denatured in 4X Protein Sample
496 Loading Buffer (Li-Cor Bioscience) under reducing conditions (NuPAGE reducing agent, Thermo
497 Fisher Scientific) at 70 °C for 10 minutes. Proteins were separated by SDS-PAGE (NuPAGE 4 to 12%
498 Bis-Tris gel; Invitrogen) and transferred to nitrocellulose membranes (Bio-Rad) using a Trans-Blot
499 Turbo Transfer system (Bio-Rad). Membranes were blocked with PBS-0.1% Tween 20 (PBS-T)
500 containing 5% milk and were incubated with rabbit monoclonal anti-CYLD (1:500, #8462 Cell
501 Signaling) and mouse monoclonal anti-β-actin (1:5,000, A5316; Sigma) diluted in blocking buffer
502 overnight at 4°C. The membranes were then incubated with anti-rabbit/mouse IgG [H+L] DyLight

503 800/680secondary antibodies diluted in blocking buffer for 1h at room temperature. Images were
504 acquired using an Odyssey CLx infrared imaging system (Li-Cor Bioscience).

505 **SARS-CoV-2 infected and bystander cell-sorting and RNA extraction on fixed samples for**
506 **RNA-seq.** A549-ACE2 cells were seeded the day prior to infection. Cells were infected with SARS-
507 CoV-2 at MOI 1 or mock infected. Infections were done in two independent repeats with three technical
508 replicates each. At 24 h post infection, cells were detached with trypsin, fixed in 4% PFA for 30 min on
509 ice and stained for spike protein as described above for flow cytometry, with RNasin added to FACS
510 buffer (1:100 dilution) just before use to prevent RNA degradation. Infected cell samples were
511 resuspended in PBS 2%, 25 mM Hepes, 5 mM EDTA (sorting buffer) and sorted at 4°C on a FACSAria
512 Fusion4L Sorter into infected (presence of S protein expression) and bystander (absence of viral protein
513 expression) cell populations. Cells were collected in FBS-coated tubes containing buffer with RNasin
514 to minimize RNA degradation. After sorting, cells were pelleted at 500g for 5 min at 4°C and RNA was
515 extracted with the RecoverAll Total Nucleic Acid Isolation Kit starting at the protease digestion step.
516 Digestion was performed for 15 min at 50°C and 15 min at 80°C in the presence of RNasin. Extraction
517 was performed according to manufacturer's instructions and the addition of RNAsin to all buffers just
518 before use until final elution of RNA in DNAse-free water. Residual DNA was further digested using
519 DNAse I (Invitrogen AM1906). RNAs were sorted at -80°C until further analysis.

520 **Library preparation, viral RNA depletion and RNA-sequencing.** 500-1000 ng of total RNA
521 were depleted of SARS-CoV-2 RNA using custom designed probes. The probes were synthesized using
522 the NC_045512.2 Wuhan-Hu-1 complete genome reference. The design was made by Illumina and is
523 composed of 459 probes, separated into two pools synthetized by IDT. For the SARS-CoV-2 depletion,
524 we mixed both pools and used 1µl of this mix per sample, replacing the Ribozero+ probes at the
525 ribodepletion reaction step of the Illumina Stranded Total RNA prep ligation protocol. The SARS-CoV-
526 2 depleted RNA samples were normalized to 300ng and ERCC Spike was added as recommended by
527 the protocol ERCC RNA Spike-In Control mixes User Guide. The libraries were prepared using the
528 Illumina Stranded mRNA Prep Ligation Reference Guide.

529 **PolyA+ RNA-sequencing analysis of sorted cells.** Dataset consists of 9 paired-end libraries (150
530 nt), 3 replicates per condition: mock, bystander and infected cells. Adaptors were trimmed with Trim
531 Galore v0.6.4 [89] (wrapper for cutadapt v2.10 [90] and FastQC v0.11.9 [91]), with options --stringency
532 5 --trim-n -q 20 --length 20 --paired --retain_unpaired. Reads were mapped to a reference containing
533 human genome (hg38), SARS-CoV-2 (NC045512.2) and ERCC sequences. STAR v2.7.3a [92] was
534 used to map the reads, with default parameters. Bam files were then filtered using SAMtools v1.10 [93]
535 to retained reads flagged as primary alignment, and with mapping quality > 30 (option -q 30 -F 0x100 -
536 F 0x800). Read coverage was computed for each strand with bamCoverage (deepTools v3.5.0 [94]) with
537 options --binSize 1 --skipNAs --filterRNAstrand forward/reverse. For the detection of unannotated
538 transcripts, Scallop v0.10.5 [35] was used to reconstruct transcripts, with options --library_type first --
539 min_transcript_coverage 2 --min_splice_bundary_hits 5 --min_flank_length 5. Scallop was run on each

540 library, and the resulting annotations were merged using cuffmerge v1.0.0 [95], with gencode annotation
541 (v32) as reference (-g option). Then BEDtools v2.29.2 [96] was used to retain only intergenic and
542 antisens transcripts regarding gencode annotation. Gene expression quantification was performed using
543 featureCounts v2.0.0 [97], with options -O -M --fraction -s 2 -p, using a merged annotation of gencode
544 v32, SARS-CoV-2 (NC045512.2), newly annotated transcripts and ERCC transcripts. Subsequent
545 analyses were performed in R v3.6.2 [98]. Differential expression analysis was performed using DESeq2
546 package [99], after filtering out genes with less than 10 raw counts for all replicates in at least one
547 condition. Gene counts were normalized on ERCC counts, using *estimateSizeFactorsForMatrix*
548 function from DESeq2. All pairwise comparisons were performed (mock vs infected, mock vs bystander
549 and bystander vs infected), and genes were retained as differential if adjusted p-value was < 0.05 and
550 log fold-change > 1 or < -1. All plots were made using custom script, except for heatmaps that were
551 done using pheatmap package (RRID:SCR_016418).

552 **PolyA+ RNA-sequencing analysis of bulk population of infected cells (from a public dataset).**
553 Fastq files produced in the study of Blanco-Melo et al (2020)[17] were retrieved from GEO repository
554 (GSE147507). Dataset consist of single-end libraries (150 nt). We compared A549-ACE2 "mock" cells
555 (SRR11517680, SRR11517681 & SRR11517682) *versus* A549-ACE2 cells infected with SARS-CoV-
556 2 at MOI 0.2 (SRR11517741, SRR11517742 & SRR11517743). Adaptors were trimmed with Trim
557 Galore v0.6.4 [89], with options --stringency 5 --trim-n -q 20 --length 20. Reads were mapped on a
558 reference containing human genome (hg38) and SARS-CoV-2 (NC045512.2) sequence. Bam files were
559 then filtered using SAMtools v1.10 [93] to retained reads flagged as primary alignment, and with
560 mapping quality > 30 (option -q 30 -F 0x100 -F 0x800). Gene expression quantification was performed
561 using featureCounts v2.0.0 [97], with options -O -M --fraction -s 2, using a merged annotation of
562 gencode v32, SARS-CoV-2 (NC045512.2) and newly annotated transcripts. Gene counts were
563 normalized on the full count matrix, using *estimateSizeFactorsForMatrix* function from DESeq2 [99].
564 Differential analysis was performed as described above.

565 **GO enrichment analysis.** The GO enrichment and KEGG pathway analysis were performed using
566 DAVID online tool (updated version 2021) [100,101]. Upregulated protein-coding genes from each
567 comparison were taken for the analysis with default background for *Homo sapiens*.
568 GOTERM_BP_DIRECT and KEGG pathway were retained and top 10 results based on adjusted p-
569 value (Benjamini) were plotted using ggplot2 R package (v 3.3.0).

570 **Identification of NF-κB target genes.** A list of coding genes that are known targets of NF-kB is
571 available on Gilmore's laboratory website (https://www.bu.edu/nf-kb/gene-resources/target-genes). We
572 selected genes from this list that were shown to be direct targets of NF-κB, and for which the gene
573 symbol could be retrieved in gencode annotation (354 genes). For identifying lncRNAs and
574 unreferenced RNAs that possess NF-κB binding site in their promoter, we used p65 ChIP-seq data from
575 GEO dataset GSE34329 [49] - one input file and 2 ChIP replicates, 38nt long reads, single-end. Reads
576 were mapped using bowtie2 v2.4.1 using hg38 as reference, and SAMtools was used to retain the one

577 flagged as primary alignment, with mapping quality > 30, and to remove PCR duplicates (markdup,
578 with -r option). NF-κB binding sites were then detected using macs2 v2.2.7.1 [102], with command
579 callpeak -t ChIP_BamFile1 ChIP_BamFile2 -c input_BamFile -f BAM -g hs -s 38 --keep-dup all. Peaks
580 in the first decile of the -log10(qvalue) value were discarded. NF-kB motif genomic coordinates in the
581 human genome were retrieved using EMBOSS fuzznuc v6.6 [103], using motif 5'-
582 G(3)[AG]N[CT](3)C(2) - 3' [104], on forward and reverse strand (option -complement Y). Peaks and
583 NF-κB motif coordinates were compared using BEDtools [96]; if a motif was contained in a peak, the
584 motif strand was assigned to the peak. LncRNA and un-references transcripts were identified as NF-κB
585 potential targets if their promoter region (1kb before transcript TSS) had a peak containing a motif or a
586 peak for which the -log10(qvalue) was in the top 5%.

587 **CUT & RUN**. The experiment was performed in monoplicate, following the protocol from
588 Henikoff Lab with some adjustments (Skene et al, 2018). Briefly, untreated cells and cells treated for
589 3h with 10 ng/mL of TNF-α were pelleted after scraping and resuspended in wash buffer (HEPES
590 20mM, NaCl 150mM, Spermidine 0.5mM) at 10^7 cells/ml. At room temperature, per sample, 10 µl of
591 Concanavalin A beads slurry washed in bead activation buffer (HEPES 20mM, KCl 10mM, $CaCl_2$ 1mM,
592 $MnCl_2$ 1mM) was added per 10^6 cells in the total volume of 1 ml of wash buffer and incubated for 10
593 min with rotation at 15–20 rpm. Antibodies against H3K27ac (Millipore, MABE647) were diluted 50
594 times, p65 (Cell Signaling, D14E12) diluted 100 times and IgG (Invitrogen, 31235) 500 times in the
595 buffer (wash buffer with 0.1% digitonin, 2 mM EDTA) and 50 µl of diluted antibody was added to the
596 cells fixed on beads and incubated for 1h. Afterward, the beads were washed twice with 250 µl of
597 digitonin buffer (wash buffer with 0.1% digitonin), resuspended in 52 µl digitonin buffer containing
598 35ng of pAG-MNase (produced at Institut Curie platform) , and incubated 10 min with agitation. Beads
599 were washed twice in 250 µl of ice-cold digitonin buffer, resuspended in 100 µl of ice-cold digitonin
600 buffer, kept on ice for 5 min before adding 2 µl of 100 mM $CaCl_2$ and incubating for 30 min on ice. The
601 reaction was stopped by addition of 100 µl of stop buffer (NaCl 340mM, EDTA 20mM, EGTA 4mM,
602 RNase A 50 µg/mL, glycogen 50 µg/mL and 0.1% digitonin) and incubated for 10 min at 37°C. Bead
603 suspension was centrifuged at 16k rcf at 4°C for 5 min and beads were recovered for DNA fragments
604 purification with NEB Monarch PCR & DNA purification kit, following the protocol enriching for short
605 DNA fragments. DNA was quantified by Qubit HS DNA kit and samples were sent for library
606 preparation and sequencing to Institut Curie's NGS platform.

607 **CUT & RUN data analysis**. Adaptors were trimmed with Trim Galore using default parameters
608 for paired-end data. Reads were aligned on human genome (hg38) using Bowtie2 (default parameters)
609 and only properly mapped reads with a mapping quality >=30 were kept. Peaks were detected using
610 macs2, with the option –keep-dup all.

611 **RNA extraction and RT-qPCR assays.** Total RNA was extracted from cells with the NucleoSpin
612 RNA II kit (Macherey-Nagel) according to the manufacturer's instructions. First-strand complementary
613 DNA (cDNA) synthesis was performed with the RevertAid H Minus M-MuLV Reverse Transcriptase

614 (Thermo Fisher Scientific) using random primers. Quantitative real-time PCR was performed on a real-
615 time PCR system (QuantStudio 6 Flex, Applied Biosystems) with Power SYBR Green RNA-to-CT 1-
616 Step Kit (Thermo Fisher Scientific). Data were analyzed using the 2-ΔΔCT method, with all samples
617 normalized to endogenous BPTF, whose gene expression was confirmed as homogenous across samples
618 by RNA-seq. Genome equivalent concentrations were determined by extrapolation from a standard
619 curve generated from serial dilutions of plasmid encoding a fragment of the RNA-dependent RNA
620 polymerase (RdRp)-IP4 of SARS-CoV-2. Primers used for RT-qPCR analysis are given in table S6.
621 **siRNA-mediated knockdown.** A549-ACE2 cells were transfected using Lipofectamine RNAiMax
622 (Life Technologies) with 10nM of control (#4390843, Ambion) or CXCL8 (L-004756-00, Dharmacon),
623 NFKB1 (L-003520-00, Dharmacon), IL32 (L-015988-00, Dharmacon), ADIRF-AS1 (siTOOLs
624 Biotech) siRNAs following the manufacturer's instructions. 48h after transfection, cells were infected
625 with SARS-CoV-2 for 24 h.
626 **Chemokine and Interferon expression and secretion.** Cell lysates for intracellular chemokine
627 quantification were obtained *via* repeated freeze-thaw cycles at -80°C of cells suspended in media
628 containing protease inhibitor cocktail (Roche Applied Science) and final centrifugation at 8000g to
629 pellet debris. IL6, CXCL1, CCL2, CXCL8 and CCL20 concentrations in supernatants of from control,
630 infected or stimulated cells, were measured using a custom-designed LEGENDplex Human Panel. Data
631 were acquired on an Attune NxT Flow Cytometer (Thermo Fisher) analyzed with LEGENDplex
632 software (BioLegend). Similarly, IFN-β, IFN-λ1 and IFN- λ2/3 concentrations were measured in
633 undiluted supernatants from control, infected or stimulated cells using a LEGENDplex Human Type
634 1/2/3 Interferon Panel assay (BioLegend) according to the manufacturer's protocol.
635 **TCID50 mediated viral titration.** A549-hACE2 cells were infected for 24 hours with MOI 1 of
636 SARS-COV-2. Virus was removed at 3hpi and fresh medium containing 2.5% FBS was added for the
637 remaining time. Supernatants were harvested the following day and stored at -80 °C until assay was
638 performed. Briefly, supernatants were 10-fold serially diluted in DMEM supplemented with 2% FBS.
639 Vero E6 cells and 50-µL potions of serially diluted virus suspensions were deposited in 96-well plate in
640 8 replicate wells. 5 days later, cells were rinsed, fixed and stained using Crystal Violet (0.2% Crystal
641 Violet in 10% Ethanol and 10% Formaldehyde) at room temperature. CPEs were assessed by calculating
642 the TCID50 values using the Spearman-Karber method [105].
643 **Statistical analysis.** Statistical parameters including the exact value of n, precision measures (as
644 means ± SEM), statistical tests and statistical significance are reported in the figure legends. In figures,
645 asterisks denote statistical significance: *$p < 0.05$, **$p < 0.01$, ***$p < 0.005$, ****$p < 0.0001$, and "ns"
646 indicates not significant. Statistical analysis was performed in GraphPad Prism 9 (GraphPad Software
647 Inc.).
648
649 **Acknowledgments**

We thank the French National Reference Centre for Respiratory Viruses hosted by Institut Pasteur (France) and headed by Pr. S. van Der Werf for providing the historical SARS-CoV-2 strain; C. Combredet and F. Tangy (Institut Pasteur) for producing and sharing MeV-GFP; H. Mouquet and C. Planchais (Institut Pasteur) for anti-S antibodies and O. Schwartz (Institut Pasteur) for the A549-ACE2 cells. We are grateful to our team member Felix Streicher for helping design the figure 2A and to all members of our laboratories for helpful discussions. We acknowledge the UTechS Immunology Platform of Institut Pasteur for the use of the cell sorter. The Biomics Platform was supported by France Génomique (ANR-10-INBS-09), IBISA and the Illumina COVID-19 Projects' offer.

Funding

This work was funded by the CNRS (NJ, AM), Institut Pasteur (NJ), 'Urgence COVID-19' fundraising campaign of Institut Pasteur (NJ), ANR-DARK COVID (AM/NJ) and DIM-1-Health (NJ/AM). DF postdoctoral fellowship was supported by the DIM-1-Health from the Conseil Régional d'Ile-de-France. SMA was supported by the Pasteur-Paris University (PPU) International PhD Program. The funders had no role in study design, data collection and analysis, decision to publish or preparation of the manuscript.

668 **References**

669 1. Wiersinga WJ, Rhodes A, Cheng AC, Peacock SJ, Prescott HC. Pathophysiology,
670 Transmission, Diagnosis, and Treatment of Coronavirus Disease 2019 (COVID-19): A Review.
671 JAMA. 2020;324: 782–793. doi:10.1001/jama.2020.12839

672 2. Trypsteen W, Cleemput JV, Snippenberg W van, Gerlo S, Vandekerckhove L. On the
673 whereabouts of SARS-CoV-2 in the human body: A systematic review. PLOS Pathogens.
674 2020;16: e1009037. doi:10.1371/journal.ppat.1009037
675 3. Chen G, Wu D, Guo W, Cao Y, Huang D, Wang H, et al. Clinical and immunological
676 features of severe and moderate coronavirus disease 2019. J Clin Invest. 2020;130: 2620–
677 2629. doi:10.1172/JCI137244
678 4. Lucas C, Wong P, Klein J, Castro TBR, Silva J, Sundaram M, et al. Longitudinal
679 analyses reveal immunological misfiring in severe COVID-19. Nature. 2020;584: 463–469.
680 doi:10.1038/s41586-020-2588-y
681 5. Giamarellos-Bourboulis EJ, Netea MG, Rovina N, Akinosoglou K, Antoniadou A,
682 Antonakos N, et al. Complex Immune Dysregulation in COVID-19 Patients with Severe
683 Respiratory Failure. Cell Host Microbe. 2020;27: 992-1000.e3.
684 doi:10.1016/j.chom.2020.04.009
685 6. Chen L, Deng H, Cui H, Fang J, Zuo Z, Deng J, et al. Inflammatory responses and
686 inflammation-associated diseases in organs. Oncotarget. 2017;9: 7204–7218.
687 doi:10.18632/oncotarget.23208
688 7. Jouvenet N, Goujon C, Banerjee A. Clash of the titans: interferons and SARS-CoV-2.
689 Trends Immunol. 2021;42: 1069–1072. doi:10.1016/j.it.2021.10.009
690 8. Streicher F, Jouvenet N. Stimulation of Innate Immunity by Host and Viral RNAs.
691 Trends in Immunology. 2019;40: 1134–1148. doi:10.1016/j.it.2019.10.009
692 9. Schneider WM, Chevillotte MD, Rice CM. Interferon-Stimulated Genes: A Complex
693 Web of Host Defenses. Annu Rev Immunol. 2014;32: 513–545. doi:10.1146/annurev-
694 immunol-032713-120231
695 10. Schoggins JW. Recent advances in antiviral interferon-stimulated gene biology.
696 F1000Res. 2018;7: 309. doi:10.12688/f1000research.12450.1
697 11. Xia H, Cao Z, Xie X, Zhang X, Chen JY-C, Wang H, et al. Evasion of Type I
698 Interferon by SARS-CoV-2. Cell Rep. 2020;33: 108234. doi:10.1016/j.celrep.2020.108234
699 12. Beyer DK, Forero A. Mechanisms of Antiviral Immune Evasion of SARS-CoV-2. J
700 Mol Biol. 2021; 167265. doi:10.1016/j.jmb.2021.167265
701 13. Sa Ribero M, Jouvenet N, Dreux M, Nisole S. Interplay between SARS-CoV-2 and
702 the type I interferon response. PLoS Pathog. 2020;16: e1008737.
703 doi:10.1371/journal.ppat.1008737
704 14. Singh M, Chazal M, Quarato P, Bourdon L, Malabat C, Vallet T, et al. A virus-derived
705 microRNA targets immune response genes during SARS-CoV-2 infection. EMBO Rep. 2021;
706 e54341. doi:10.15252/embr.202154341
707 15. Pawlica P, Yario TA, White S, Wang J, Moss WN, Hui P, et al. SARS-CoV-2
708 expresses a microRNA-like small RNA able to selectively repress host genes. PNAS.
709 2021;118. doi:10.1073/pnas.2116668118
710 16. Hadjadj J, Yatim N, Barnabei L, Corneau A, Boussier J, Smith N, et al. Impaired type
711 I interferon activity and inflammatory responses in severe COVID-19 patients. Science.
712 2020;369: 718–724. doi:10.1126/science.abc6027
713 17. Blanco-Melo D, Nilsson-Payant BE, Liu W-C, Uhl S, Hoagland D, Møller R, et al.
714 Imbalanced Host Response to SARS-CoV-2 Drives Development of COVID-19. Cell.
715 2020;181: 1036-1045.e9. doi:10.1016/j.cell.2020.04.026

716 18. Finkel Y, Gluck A, Nachshon A, Winkler R, Fisher T, Rozman B, et al. SARS-CoV-2
717 uses a multipronged strategy to impede host protein synthesis. Nature. 2021;594: 240–245.
718 doi:10.1038/s41586-021-03610-3
719 19. Wyler E, Mösbauer K, Franke V, Diag A, Gottula LT, Arsiè R, et al. Transcriptomic
720 profiling of SARS-CoV-2 infected human cell lines identifies HSP90 as target for COVID-19
721 therapy. iScience. 2021;24: 102151. doi:10.1016/j.isci.2021.102151
722 20. Xiong Y, Liu Y, Cao L, Wang D, Guo M, Jiang A, et al. Transcriptomic
723 characteristics of bronchoalveolar lavage fluid and peripheral blood mononuclear cells in
724 COVID-19 patients. Emerg Microbes Infect. 2020;9: 761–770.
725 doi:10.1080/22221751.2020.1747363
726 21. Carlin AF, Vizcarra EA, Branche E, Viramontes KM, Suarez-Amaran L, Ley K, et al.
727 Deconvolution of pro- and antiviral genomic responses in Zika virus-infected and bystander
728 macrophages. Proc Natl Acad Sci U S A. 2018;115: E9172–E9181.
729 doi:10.1073/pnas.1807690115
730 22. Triana S, Metz-Zumaran C, Ramirez C, Kee C, Doldan P, Shahraz M, et al. Single-cell
731 analyses reveal SARS-CoV-2 interference with intrinsic immune response in the human gut.
732 Molecular Systems Biology. 2021;17: e10232. doi:10.15252/msb.202110232
733 23. Fiege JK, Thiede JM, Nanda HA, Matchett WE, Moore PJ, Montanari NR, et al.
734 Single cell resolution of SARS-CoV-2 tropism, antiviral responses, and susceptibility to
735 therapies in primary human airway epithelium. PLoS Pathog. 2021;17: e1009292.
736 doi:10.1371/journal.ppat.1009292
737 24. Ravindra NG, Alfajaro MM, Gasque V, Huston NC, Wan H, Szigeti-Buck K, et al.
738 Single-cell longitudinal analysis of SARS-CoV-2 infection in human airway epithelium
739 identifies target cells, alterations in gene expression, and cell state changes. PLOS Biology.
740 2021;19: e3001143. doi:10.1371/journal.pbio.3001143
741 25. Liao M, Liu Y, Yuan J, Wen Y, Xu G, Zhao J, et al. Single-cell landscape of
742 bronchoalveolar immune cells in patients with COVID-19. Nat Med. 2020;26: 842–844.
743 doi:10.1038/s41591-020-0901-9
744 26. Chen G, Ning B, Shi T. Single-Cell RNA-Seq Technologies and Related
745 Computational Data Analysis. Front Genet. 2019;10: 317. doi:10.3389/fgene.2019.00317
746 27. Zhang MJ, Ntranos V, Tse D. Determining sequencing depth in a single-cell RNA-seq
747 experiment. Nat Commun. 2020;11: 774. doi:10.1038/s41467-020-14482-y
748 28. Kopp F, Mendell JT. Functional Classification and Experimental Dissection of Long
749 Noncoding RNAs. Cell. 2018;172: 393–407. doi:10.1016/j.cell.2018.01.011
750 29. Iyer MK, Niknafs YS, Malik R, Singhal U, Sahu A, Hosono Y, et al. The landscape of
751 long noncoding RNAs in the human transcriptome. Nat Genet. 2015;47: 199–208.
752 doi:10.1038/ng.3192
753 30. Encode Project Consortium. An integrated encyclopedia of DNA elements in the
754 human genome. Nature. 2012;489: 57–74. doi:10.1038/nature11247
755 31. Guttman M, Amit I, Garber M, French C, Lin MF, Feldser D, et al. Chromatin
756 signature reveals over a thousand highly conserved large non-coding RNAs in mammals.
757 Nature. 2009;458: 223–7. doi:10.1038/nature07672
758 32. Meng XY, Luo Y, Anwar MN, Sun Y, Gao Y, Zhang H, et al. Long Non-Coding
759 RNAs: Emerging and Versatile Regulators in Host-Virus Interactions. Front Immunol.
760 2017;8: 1663. doi:10.3389/fimmu.2017.01663
761 33. Carnero E, Barriocanal M, Segura V, Guruceaga E, Prior C, Borner K, et al. Type I
762 Interferon Regulates the Expression of Long Non-Coding RNAs. Front Immunol. 2014;5:
763 548. doi:10.3389/fimmu.2014.00548
764 34. Basavappa MG, Ferretti M, Dittmar M, Stoute J, Sullivan MC, Whig K, et al. The
765 lncRNA ALPHA specifically targets chikungunya virus to control infection. Molecular Cell.

766 2022;82: 3729-3744.e10. doi:10.1016/j.molcel.2022.08.030
767 35. Shao M, Kingsford C. Accurate assembly of transcripts through phase-preserving
768 graph decomposition. Nat Biotechnol. 2017;35: 1167–1169. doi:10.1038/nbt.4020
769 36. Nilsson-Payant BE, Uhl S, Grimont A, Doane AS, Cohen P, Patel RS, et al. The NF-
770 κB Transcriptional Footprint Is Essential for SARS-CoV-2 Replication. J Virol. 2021;95:
771 e0125721. doi:10.1128/JVI.01257-21
772 37. Neufeldt CJ, Cerikan B, Cortese M, Frankish J, Lee J-Y, Plociennikowska A, et al.
773 SARS-CoV-2 infection induces a pro-inflammatory cytokine response through cGAS-STING
774 and NF-κB. Commun Biol. 2022;5: 1–15. doi:10.1038/s42003-021-02983-5
775 38. Herter EK, Li D, Toma MA, Vij M, Li X, Visscher D, et al. WAKMAR2, a Long
776 Noncoding RNA Downregulated in Human Chronic Wounds, Modulates Keratinocyte
777 Motility and Production of Inflammatory Chemokines. Journal of Investigative Dermatology.
778 2019;139: 1373–1384. doi:10.1016/j.jid.2018.11.033
779 39. Zhu X, Liu Y, Yu J, Du J, Guo R, Feng Y, et al. LncRNA HOXA-AS2 represses
780 endothelium inflammation by regulating the activity of NF-κB signaling. Atherosclerosis.
781 2019;281: 38–46. doi:10.1016/j.atherosclerosis.2018.12.012
782 40. Liu B, Sun L, Liu Q, Gong C, Yao Y, Lv X, et al. A Cytoplasmic NF-κB Interacting
783 Long Noncoding RNA Blocks IκB Phosphorylation and Suppresses Breast Cancer Metastasis.
784 Cancer Cell. 2015;27: 370–381. doi:10.1016/j.ccell.2015.02.004
785 41. Santoro MG, Rossi A, Amici C. NF-kappaB and virus infection: who controls whom.
786 EMBO J. 2003;22: 2552–2560. doi:10.1093/emboj/cdg267
787 42. Aggarwal BB. Signalling pathways of the TNF superfamily: a double-edged sword.
788 Nat Rev Immunol. 2003;3: 745–756. doi:10.1038/nri1184
789 43. Banerjee AK, Blanco MR, Bruce EA, Honson DD, Chen LM, Chow A, et al. SARS-
790 CoV-2 Disrupts Splicing, Translation, and Protein Trafficking to Suppress Host Defenses.
791 Cell. 2020;183: 1325-1339.e21. doi:10.1016/j.cell.2020.10.004
792 44. Lapointe CP, Grosely R, Johnson AG, Wang J, Fernández IS, Puglisi JD. Dynamic
793 competition between SARS-CoV-2 NSP1 and mRNA on the human ribosome inhibits
794 translation initiation. Proc Natl Acad Sci U S A. 2021;118: e2017715118.
795 doi:10.1073/pnas.2017715118
796 45. Yuan S, Peng L, Park JJ, Hu Y, Devarkar SC, Dong MB, et al. Nonstructural Protein 1
797 of SARS-CoV-2 Is a Potent Pathogenicity Factor Redirecting Host Protein Synthesis
798 Machinery toward Viral RNA. Mol Cell. 2020;80: 1055-1066.e6.
799 doi:10.1016/j.molcel.2020.10.034
800 46. Helin E, Vainionpää R, Hyypiä T, Julkunen I, Matikainen S. Measles virus activates
801 NF-kappa B and STAT transcription factors and production of IFN-alpha/beta and IL-6 in the
802 human lung epithelial cell line A549. Virology. 2001;290: 1–10. doi:10.1006/viro.2001.1174
803 47. Oeckinghaus A, Ghosh S. The NF-κB Family of Transcription Factors and Its
804 Regulation. Cold Spring Harb Perspect Biol. 2009;1: a000034.
805 doi:10.1101/cshperspect.a000034
806 48. Ten RM, Paya CV, Israël N, Le Bail O, Mattei MG, Virelizier JL, et al. The
807 characterization of the promoter of the gene encoding the p50 subunit of NF-kappa B
808 indicates that it participates in its own regulation. EMBO J. 1992;11: 195–203.
809 49. Raskatov JA, Meier JL, Puckett JW, Yang F, Ramakrishnan P, Dervan PB.
810 Modulation of NF-κB-dependent gene transcription using programmable DNA minor groove
811 binders. Proc Natl Acad Sci U S A. 2012;109: 1023–1028. doi:10.1073/pnas.1118506109
812 50. Krawczyk M, Emerson BM. p50-associated COX-2 extragenic RNA (PACER)
813 activates COX-2 gene expression by occluding repressive NF-κB complexes. Elife. 2014;3:
814 e01776. doi:10.7554/eLife.01776
815 51. Kovalenko A, Chable-Bessia C, Cantarella G, Israël A, Wallach D, Courtois G. The

816 tumour suppressor CYLD negatively regulates NF-kappaB signalling by deubiquitination.
817 Nature. 2003;424: 801–805. doi:10.1038/nature01802
818 52. Murgolo N, Therien AG, Howell B, Klein D, Koeplinger K, Lieberman LA, et al.
819 SARS-CoV-2 tropism, entry, replication, and propagation: Considerations for drug discovery
820 and development. PLOS Pathogens. 2021;17: e1009225. doi:10.1371/journal.ppat.1009225
821 53. Zhang K, Miorin L, Makio T, Dehghan I, Gao S, Xie Y, et al. Nsp1 protein of SARS-
822 CoV-2 disrupts the mRNA export machinery to inhibit host gene expression. Science
823 Advances. 2021 [cited 6 Feb 2022]. doi:10.1126/sciadv.abe7386
824 54. Huang C, Lokugamage KG, Rozovics JM, Narayanan K, Semler BL, Makino S.
825 SARS coronavirus nsp1 protein induces template-dependent endonucleolytic cleavage of
826 mRNAs: viral mRNAs are resistant to nsp1-induced RNA cleavage. PLoS Pathog. 2011;7:
827 e1002433. doi:10.1371/journal.ppat.1002433
828 55. Kamitani W, Huang C, Narayanan K, Lokugamage KG, Makino S. A two-pronged
829 strategy to suppress host protein synthesis by SARS coronavirus Nsp1 protein. Nat Struct Mol
830 Biol. 2009;16: 1134–1140. doi:10.1038/nsmb.1680
831 56. Kamitani W, Narayanan K, Huang C, Lokugamage K, Ikegami T, Ito N, et al. Severe
832 acute respiratory syndrome coronavirus nsp1 protein suppresses host gene expression by
833 promoting host mRNA degradation. PNAS. 2006;103: 12885–12890.
834 doi:10.1073/pnas.0603144103
835 57. Mendez AS, Ly M, González-Sánchez AM, Hartenian E, Ingolia NT, Cate JH, et al.
836 The N-terminal domain of SARS-CoV-2 nsp1 plays key roles in suppression of cellular gene
837 expression and preservation of viral gene expression. Cell Reports. 2021;37: 109841.
838 doi:10.1016/j.celrep.2021.109841
839 58. Sun G, Cui Q, Garcia G, Wang C, Zhang M, Arumugaswami V, et al. Comparative
840 transcriptomic analysis of SARS-CoV-2 infected cell model systems reveals differential
841 innate immune responses. Sci Rep. 2021;11: 17146. doi:10.1038/s41598-021-96462-w
842 59. Mu J, Fang Y, Yang Q, Shu T, Wang A, Huang M, et al. SARS-CoV-2 N protein
843 antagonizes type I interferon signaling by suppressing phosphorylation and nuclear
844 translocation of STAT1 and STAT2. Cell Discov. 2020;6: 1–4. doi:10.1038/s41421-020-
845 00208-3
846 60. Miorin L, Kehrer T, Sanchez-Aparicio MT, Zhang K, Cohen P, Patel RS, et al. SARS-
847 CoV-2 Orf6 hijacks Nup98 to block STAT nuclear import and antagonize interferon
848 signaling. Proc Natl Acad Sci U S A. 2020;117: 28344–28354. doi:10.1073/pnas.2016650117
849 61. Rebendenne A, Valadão ALC, Tauziet M, Maarifi G, Bonaventure B, McKellar J, et
850 al. SARS-CoV-2 triggers an MDA-5-dependent interferon response which is unable to control
851 replication in lung epithelial cells. J Virol. 2021; JVI.02415-20. doi:10.1128/JVI.02415-20
852 62. Banerjee A, El-Sayes N, Budylowski P, Jacob RA, Richard D, Maan H, et al.
853 Experimental and natural evidence of SARS-CoV-2-infection-induced activation of type I
854 interferon responses. iScience. 2021;24: 102477. doi:10.1016/j.isci.2021.102477
855 63. Yin X, Riva L, Pu Y, Martin-Sancho L, Kanamune J, Yamamoto Y, et al. MDA5
856 Governs the Innate Immune Response to SARS-CoV-2 in Lung Epithelial Cells. Cell Rep.
857 2021;34: 108628. doi:10.1016/j.celrep.2020.108628
858 64. Lei X, Dong X, Ma R, Wang W, Xiao X, Tian Z, et al. Activation and evasion of type
859 I interferon responses by SARS-CoV-2. Nat Commun. 2020;11: 3810. doi:10.1038/s41467-
860 020-17665-9
861 65. Stanifer ML, Kee C, Cortese M, Zumaran CM, Triana S, Mukenhirn M, et al. Critical
862 Role of Type III Interferon in Controlling SARS-CoV-2 Infection in Human Intestinal
863 Epithelial Cells. Cell Reports. 2020;32: 107863. doi:10.1016/j.celrep.2020.107863
864 66. Lamers MM, van der Vaart J, Knoops K, Riesebosch S, Breugem TI, Mykytyn AZ, et
865 al. An organoid-derived bronchioalveolar model for SARS-CoV-2 infection of human

alveolar type II-like cells. EMBO J. 2021;40: e105912. doi:10.15252/embj.2020105912
67. Stanifer ML, Kee C, Cortese M, Zumaran CM, Triana S, Mukenhirn M, et al. Critical Role of Type III Interferon in Controlling SARS-CoV-2 Infection in Human Intestinal Epithelial Cells. Cell Rep. 2020;32: 107863. doi:10.1016/j.celrep.2020.107863
68. Deng L, Zeng Q, Wang M, Cheng A, Jia R, Chen S, et al. Suppression of NF-κB Activity: A Viral Immune Evasion Mechanism. Viruses. 2018;10: E409. doi:10.3390/v10080409
69. Neufeldt CJ, Cerikan B, Cortese M, Frankish J, Lee J-Y, Plociennikowska A, et al. SARS-CoV-2 infection induces a pro-inflammatory cytokine response through cGAS-STING and NF-κB. 2020 Jul p. 2020.07.21.212639. doi:10.1101/2020.07.21.212639
70. Su C-M, Wang L, Yoo D. Activation of NF-κB and induction of proinflammatory cytokine expressions mediated by ORF7a protein of SARS-CoV-2. Sci Rep. 2021;11: 13464. doi:10.1038/s41598-021-92941-2
71. Li T, Kenney AD, Liu H, Fiches GN, Zhou D, Biswas A, et al. SARS-CoV-2 Nsp14 activates NF-κB signaling and induces IL-8 upregulation. bioRxiv. 2021; 2021.05.26.445787. doi:10.1101/2021.05.26.445787
72. Li W, Qiao J, You Q, Zong S, Peng Q, Liu Y, et al. SARS-CoV-2 Nsp5 Activates NF-κB Pathway by Upregulating SUMOylation of MAVS. Frontiers in Immunology. 2021;12: 4681. doi:10.3389/fimmu.2021.750969
73. Boreika R, Sitkauskiene B. Interleukin-32 in Pathogenesis of Atopic Diseases: Proinflammatory or Anti-Inflammatory Role? Journal of Interferon & Cytokine Research. 2021;41: 235–243. doi:10.1089/jir.2020.0230
74. Li Y, Xie J, Xu X, Liu L, Wan Y, Liu Y, et al. Inducible Interleukin 32 (IL-32) Exerts Extensive Antiviral Function via Selective Stimulation of Interferon λ1 (IFN-λ1) *. Journal of Biological Chemistry. 2013;288: 20927–20941. doi:10.1074/jbc.M112.440115
75. Nold MF, Nold-Petry CA, Pott GB, Zepp JA, Saavedra MT, Kim S-H, et al. Endogenous IL-32 controls cytokine and HIV-1 production. J Immunol. 2008;181: 557–565. doi:10.4049/jimmunol.181.1.557
76. Li W, Sun W, Liu L, Yang F, Li Y, Chen Y, et al. IL-32: A Host Proinflammatory Factor against Influenza Viral Replication Is Upregulated by Aberrant Epigenetic Modifications during Influenza A Virus Infection. The Journal of Immunology. 2010;185: 5056–5065. doi:10.4049/jimmunol.0902667
77. Kim S-H, Han S-Y, Azam T, Yoon D-Y, Dinarello CA. Interleukin-32: a cytokine and inducer of TNFalpha. Immunity. 2005;22: 131–142. doi:10.1016/j.immuni.2004.12.003
78. Khabar KSA, Al-Zoghaibi F, Al-Ahdal MN, Murayama T, Dhalla M, Mukaida N, et al. The α Chemokine, Interleukin 8, Inhibits the Antiviral Action of Interferon α. J Exp Med. 1997;186: 1077–1085.
79. Pollicino T, Bellinghieri L, Restuccia A, Raffa G, Musolino C, Alibrandi A, et al. Hepatitis B virus (HBV) induces the expression of interleukin-8 that in turn reduces HBV sensitivity to interferon-alpha. Virology. 2013;444: 317–328. doi:10.1016/j.virol.2013.06.028
80. Kambara H, Niazi F, Kostadinova L, Moonka DK, Siegel CT, Post AB, et al. Negative regulation of the interferon response by an interferon-induced long non-coding RNA. Nucleic Acids Res. 2014;42: 10668–80. doi:10.1093/nar/gku713
81. Peng X, Gralinski L, Armour CD, Ferris MT, Thomas MJ, Proll S, et al. Unique signatures of long noncoding RNA expression in response to virus infection and altered innate immune signaling. MBio. 2010;1. doi:10.1128/mBio.00206-10
82. Ouyang J, Zhu X, Chen Y, Wei H, Chen Q, Chi X, et al. NRAV, a long noncoding RNA, modulates antiviral responses through suppression of interferon-stimulated gene transcription. Cell Host Microbe. 2014;16: 616–26. doi:10.1016/j.chom.2014.10.001
83. Du M, Yuan L, Tan X, Huang D, Wang X, Zheng Z, et al. The LPS-inducible lncRNA

916 Mirt2 is a negative regulator of inflammation. Nat Commun. 2017;8: 2049.
917 doi:10.1038/s41467-017-02229-1
918 84. Meydan C, Madrer N, Soreq H. The Neat Dance of COVID-19: NEAT1, DANCR,
919 and Co-Modulated Cholinergic RNAs Link to Inflammation. Frontiers in Immunology.
920 2020;11. Available: https://www.frontiersin.org/article/10.3389/fimmu.2020.590870
921 85. Saha C, Laha S, Chatterjee R, Bhattacharyya NP. Co-Regulation of Protein Coding
922 Genes by Transcription Factor and Long Non-Coding RNA in SARS-CoV-2 Infected Cells:
923 An In Silico Analysis. Noncoding RNA. 2021;7: 74. doi:10.3390/ncrna7040074
924 86. Vishnubalaji R, Shaath H, Alajez NM. Protein Coding and Long Noncoding RNA
925 (lncRNA) Transcriptional Landscape in SARS-CoV-2 Infected Bronchial Epithelial Cells
926 Highlight a Role for Interferon and Inflammatory Response. Genes (Basel). 2020;11: E760.
927 doi:10.3390/genes11070760
928 87. Mukherjee S, Banerjee B, Karasik D, Frenkel-Morgenstern M. mRNA-lncRNA Co-
929 Expression Network Analysis Reveals the Role of lncRNAs in Immune Dysfunction during
930 Severe SARS-CoV-2 Infection. Viruses. 2021;13: 402. doi:10.3390/v13030402
931 88. Combredet C, Labrousse V, Mollet L, Lorin C, Delebecque F, Hurtrel B, et al. A
932 Molecularly Cloned Schwarz Strain of Measles Virus Vaccine Induces Strong Immune
933 Responses in Macaques and Transgenic Mice. Journal of Virology. 2003;77: 11546–11554.
934 doi:10.1128/JVI.77.21.11546-11554.2003
935 89. Babraham Bioinformatics - Trim Galore! [cited 21 Feb 2022]. Available:
936 https://www.bioinformatics.babraham.ac.uk/projects/trim_galore/
937 90. Babraham Bioinformatics - FastQC A Quality Control tool for High Throughput
938 Sequence Data. [cited 21 Feb 2022]. Available:
939 https://www.bioinformatics.babraham.ac.uk/projects/fastqc/
940 91. Martin M. Cutadapt removes adapter sequences from high-throughput sequencing
941 reads. EMBnet.journal. 2011;17: 10–12. doi:http://dx.doi.org/10.14806/ej.17.1.200
942 92. Dobin A, Davis CA, Schlesinger F, Drenkow J, Zaleski C, Jha S, et al. STAR:
943 ultrafast universal RNA-seq aligner. Bioinformatics. 2013;29: 15–21.
944 doi:10.1093/bioinformatics/bts635
945 93. Li H, Handsaker B, Wysoker A, Fennell T, Ruan J, Homer N, et al. The Sequence
946 Alignment/Map format and SAMtools. Bioinformatics. 2009;25: 2078–9.
947 doi:10.1093/bioinformatics/btp352
948 94. Ramírez F, Ryan DP, Grüning B, Bhardwaj V, Kilpert F, Richter AS, et al.
949 deepTools2: a next generation web server for deep-sequencing data analysis. Nucleic Acids
950 Res. 2016;44: W160-165. doi:10.1093/nar/gkw257
951 95. Trapnell C, Williams BA, Pertea G, Mortazavi A, Kwan G, van Baren MJ, et al.
952 Transcript assembly and quantification by RNA-Seq reveals unannotated transcripts and
953 isoform switching during cell differentiation. Nat Biotechnol. 2010;28: 511–515.
954 doi:10.1038/nbt.1621
955 96. Quinlan AR, Hall IM. BEDTools: a flexible suite of utilities for comparing genomic
956 features. Bioinformatics. 2010;26: 841–2. doi:10.1093/bioinformatics/btq033
957 97. Liao Y, Smyth GK, Shi W. featureCounts: an efficient general purpose program for
958 assigning sequence reads to genomic features. Bioinformatics. 2014;30: 923–930.
959 doi:10.1093/bioinformatics/btt656
960 98. R Core Team. R: A Language and Environment for Statistical Computing. Vienna,
961 Austria; 2017.
962 99. Love MI, Huber W, Anders S. Moderated estimation of fold change and dispersion for
963 RNA-seq data with DESeq2. Genome Biol. 2014;15: 550. doi:10.1186/s13059-014-0550-8
964 100. Huang DW, Sherman BT, Lempicki RA. Systematic and integrative analysis of large
965 gene lists using DAVID bioinformatics resources. Nat Protoc. 2009;4: 44–57.

966 doi:10.1038/nprot.2008.211
967 101. Huang DW, Sherman BT, Lempicki RA. Bioinformatics enrichment tools: paths
968 toward the comprehensive functional analysis of large gene lists. Nucleic Acids Res. 2009;37:
969 1–13. doi:10.1093/nar/gkn923
970 102. Zhang Y, Liu T, Meyer CA, Eeckhoute J, Johnson DS, Bernstein BE, et al. Model-
971 based Analysis of ChIP-Seq (MACS). Genome Biology. 2008;9: R137. doi:10.1186/gb-2008-
972 9-9-r137
973 103. EMBOSS: fuzznuc. [cited 21 Feb 2022]. Available: http://emboss.toulouse.inra.fr/cgi-
974 bin/emboss/fuzznuc
975 104. Chen FE, Huang DB, Chen YQ, Ghosh G. Crystal structure of p50/p65 heterodimer of
976 transcription factor NF-kappaB bound to DNA. Nature. 1998;391: 410–413.
977 doi:10.1038/34956
978 105. Aicher S-M, Streicher F, Chazal M, Planas D, Luo D, Buchrieser J, et al. Species-
979 Specific Molecular Barriers to SARS-CoV-2 Replication in Bat Cells. J Virol. 2022;96:
980 e0060822. doi:10.1128/jvi.00608-22
981
982

983

984 **Figure legends**

985

986 **Figure 1**. Differential transcriptomic analysis of SARS-CoV-2 infected and bystander lung cells. (**A**)
987 Scheme summarizing the experimental workflow. A549-ACE2 cells were infected with SARS-CoV-2
988 at a MOI of 1 for 24h, stained for viral S protein followed by flow cytometry sorting of productively
989 infected (S+) and bystander (S-) cells. Total RNA from mock, S- and S+ cells was depleted of ribosomal
990 and viral RNAs and sequenced. (**B**) Representative FACS plot of S protein staining used for sorting
991 productively infected cells. (**C**) Percentage of reads in libraries originating from human genome or
992 SARS-CoV-2 sequence, before and after depletion of viral reads. (**D**) PCA plot based on the top 500
993 most variable genes between mock, bystander (S-) and infected (S+) cells. (**E**) Volcano plots presenting
994 distri- bution of classes of transcripts (mRNA-blue, lncRNA-red, unannotated-green) based on their
995 log2 fold-change for 3 comparisons: infected cells vs mock, infected cells vs bystander and bystander
996 vs mock. (**F**) Heatmaps presenting z-score of log2 normalized counts for all differentially expressed
997 genes between mock, bystander and infected cells, separated for mRNAs, lncRNAs and unannotated
998 RNA.

999 **Figure 2**. Separating lung cells based on the expression of the viral S protein improved discovery of
1000 DEGs. (**A**) Venn diagram repre- senting gene overlap between DE-seq from sorted vs mock samples
1001 and mixed vs mock data re-analyzed from Blanco-Melo et al. 2020 (MOI of 0.2). The genes were
1002 defined as upregulated if log2 fold change was equal or above 1 (right panel) and equal or below -1 for
1003 downregulated genes (left panel). Genes were defined as expressed when they were represented by at
1004 least 10 normalized reads in each replicate. The solid lines and central overlap show the genes that
1005 appear in both datasets while dashed gray zones outline genes detected in only one of the two datasets.
1006 (**B**) RT-qPCR quantification of viral genome copy number per µg of total RNA extrac- ted from A549-
1007 ACE2 cells infected by SARS-CoV-2 at a MOI of 1, analyzed either in bulk (left side of graph, n=2
1008 independent expe- riments, line at mean) or post-sorting based on Spike protein expression, allowing
1009 distinction between productively infected and bystander subpopulations (right side of graph, n=3
1010 experiments, line at mean). (**C-D**) RT-qPCR quantification of mRNA, lncRNA, and unannotated-RNA,
1011 that were identified as upregulated (**C**) or downregulated (**D**) upon infection by SARS-CoV-2 in the
1012 RNA-seq analysis, in total RNA extracted from A549-ACE2 cells infected with SARS-CoV-2 at a MOI
1013 of 1, analyzed either in bulk (left side of graph) or post-sorting based on Spike protein expression (right
1014 side of graph, normalized fold change over mock-infec- ted, n=3 independent experiments, ratio-paired
1015 t test, line at mean ± SEM). (**E**) Top 10 enriched GO terms for Biological Process (BP) and KEGG
1016 pathways from DAVID database ranked by the adjusted p-value (Benjamini), for upregulated mRNAs
1017 identified in RNA-Seq comparison between infected vs mock cells.

1018 **Figure 3**. Inflammatory cytokines, but not IFNs, are produced and secreted by infected cells. (**A**)
1019 Quantification of the indicated chemokines by cytometry bead array in A549-ACE2 cell lysates obtained
1020 24 hours post mock-infection or infected with SARS-CoV-2 at a MOI of 1, or post-treatment with
1021 transfectant alone or in combination with 10 ng/μL of Poly(I:C) (n=3 independent experiments, paired
1022 One-Way ANOVA with Turkey's post-test, line at mean ± SEM). (**B**) Quantification of the indicated
1023 chemokines by cytometry bead array in supernatant (SN) of cells shown in (A) (n=3 independent
1024 experiments, paired One-Way ANOVA with Turkey's post-test, line at mean ± SEM). (**C**) Percentages
1025 of infected A549-ACE2 cells 24 hours post infection (MOI of 1) with SARS-CoV-2 or Measles virus
1026 expressing GFP (MeV), quantified by flow cytometry using Spike protein staining and GFP expression,
1027 respectively (n=3 independent experiments, line at mean ± SEM). (**D**) Quantification of secretion of
1028 IFNβ, IFNλ1 and IFNλ2/3 by cytometry bead arrays in supernatant of A549-ACE2 cells 24 hours post-
1029 infection with SARS-CoV-2 or MeV (MOI of 1), or post-treatment with transfectant alone or in
1030 combination with 10 ng/μL of Poly(I:C) (n=3 independent experiments, One-Way ANOVA with
1031 Šídák's post-test, line at mean ± SEM). ULOD: Upper Limit of Detection; LLOD: Lower Limit of
1032 Detection.

1033 **Figure 4.** Upregulated NF-κB target genes contribute to an optimal SARS-CoV-2 replication. (**A**)
1034 Volcano plot presenting log2 fold change of RNA expression from RNA-seq analysis between S+ and
1035 mock cells and showing known NF-κB target mRNAs (labeled in blue), as well as NF-κB target
1036 lncRNAs (red) and unannotated RNAs (green) predicted from ChIP and motif analysis. (**B**) Volcano
1037 plot presenting log2 fold change of RNA expression from RNA-seq analysis between S+ and mock cells
1038 and showing DEGs with peaks of upstream p65 binding, observed via Cut&Run performed after 3 hours
1039 TNFα treatment. (**C**) RT-qPCR quantification of knock-down efficiency of indicated transcripts in
1040 A549-ACE2 cells, 48 hours post-transfection with a pool of siRNAs targeting indicated genes
1041 (normalized fold change over control siRNA, n=3 independent experiments, ratio-paired t test, line at
1042 mean ± SEM). (**D**) RT-qPCR quantification of viral genome copy number per μg of total RNA extracted
1043 from A549-ACE2 cells, with indicated genes knocked down, 24 hours after infection with SARS-CoV-
1044 2 (MOI of 1) (n=3 independent experiments, One-Way ANOVA with Dunnett's post-test, line at mean
1045 ± SEM). (**E**) Percentages of infected A549-ACE2 cells, with selected genes knocked-down, 24 hours
1046 post infection with SARS-CoV-2 (MOI of 1), quantified by flow cytometry using Spike protein staining
1047 (n=3 independent experiments, mixed model one-Way ANOVA with Dunnett's post-test, line at mean
1048 ± SEM). (**F**) Viral titers in cell supernatants of A549-ACE2 cells, with indicated genes knocked down,
1049 24 hours after infection with SARS-CoV-2 (MOI of 1) (n=3 independent experiments, One-way
1050 ANOVA performed on Log-transformed data, with Dunnett's post-test, line at mean ± SEM). Titers
1051 were determined by calculation of TCID50 using the Spearman-Karber Method.

1052 **Figure 5.** Identification of CYLD gene as a regulator of SARS-CoV-2 infection and inflammation (**A**)
1053 Visualization of read coverage (tag/nucleotide) from polyA+ RNA-seq (red, blue, grey), Cut&Run
1054 sequencing (green) and ChIP-seq (IP – Input, yellow) at CYLD-AS1 locus. RNA-seq, Cut&Run-seq
1055 and ChIP-seq data were normalized independently. (**B**) RT-qPCR quantification of knock-down
1056 efficiency of CYLD transcript in A549-ACE2 cells, 72 hours post-transfection with indicated siRNA
1057 pools and 24h post-infection with SARS-CoV-2 (MOI of 1) (normalized fold change over control
1058 siRNA, n=3 independent experiments, paired One-Way ANOVA with Sidak's post-test performed on
1059 non-normalized ΔCt values, line at mean ± SEM). (**C**) Western Blot showing efficient knockdown of
1060 CYLD protein, 48h post-transfection with Ctrl siRNA pool and siRNA pool targeting CYLD transcript.
1061 (**D**) Percentages of infected A549-ACE2 cells, with selected genes knocked-down, 24 hours post
1062 infection with SARS-CoV-2 (MOI of 1), quantified by flow cytometry using Spike protein staining (n=3
1063 independent experiments, paired t-test, line at mean ± SEM). (**E**) RT-qPCR quantification of transcript
1064 induction of indicated genes in A549-ACE2 cells, 72 hours post-transfection with indicated siRNA
1065 pools and 24h post-infection with SARS-CoV-2 (MOI of 1) (normalized fold change over mock-
1066 infected, control siRNA, n=3 independent experiments, paired One-Way ANOVA with Sidak's post-
1067 test performed on non-normalized ΔCt values, line at mean ± SEM). (**F**) Quantification of secretion of
1068 IL-6, CCL-2 and IL-8 by cytometry bead arrays in supernatant of A549-ACE2 cells, 72 hours post-
1069 transfection with indicated siRNA pools and 24h post-infection with SARS-CoV-2 (MOI of 1) (n=3
1070 independent experiments, ratio-paired t-test, line at mean ± SEM). (**G**) Working model: CYLD acts by
1071 dampening the release of inflammatory cytokines via negative regulation of the NF-κB pathway (left).
1072 Reduced expression levels of CYLD (right) lead to increased inflammation and enhanced SARS-CoV-
1073 2 infection (Created with BioRender.com).
1074

1075 **Supplementary figure legends**

1076 **Figure S1**. (**A-B**) Heatmaps presenting z-score of log2 normalized counts for differentially expressed
1077 genes between (**A**) S+ vs S- cells or (**B**) S- vs mock-infected treated cells, separated for mRNAs,
1078 lncRNAs and unannotated RNAs. (**C**) Heatmap showing expression of IFN genes as normalized read
1079 counts (log2) of the IFN genes for all replicates in mock, bystander & infected cells. The "de.gene" color
1080 scale represents the differentially expressed genes between infected and mock conditions, with
1081 "no_exprs" value for genes that were not tested because gene expression was too weak. The
1082 "p65.in.prom" color scale indicates whether a gene has a Cut & Run peak (upon TNFα stimulation) in
1083 its promoter.

1084 **Figure S2**. MA plot showing the response to infection of an artificially reconstructed mixed cell
1085 population (80% bystander, 20% infected, left) compared to cells sorted based on the expression of the
1086 viral protein Spike (infected, middle; bystander, right).

1087 **Figure S3**. (**A**) Visualization of read coverage (tag/nucleotide) from polyA+ RNA-seq normalized on
1088 ERCC reads for IL32, WAKMAR2, FEN1 and AC016747.1. (**B-C**) RT-qPCR quantification of mRNAs
1089 and lncRNAs that are either upregulated (**B**) or downregulated (**C**) upon infection with SARS-CoV-2,
1090 in total RNA extracted from A549-ACE2 cells infected at an MOI of 1, analyzed either in bulk (left side
1091 of graph) or post sorting based on Spike protein (right side of graph, normalized fold change over mock-
1092 infected, n=3 independent experiments, ratio-paired t test, line at mean ± SEM).

1093 **Figure S4**. (**A**) RT-qPCR quantification of transcript induction of indicated chemokines in A549-ACE2
1094 cells, 24 hours post infection with SARS-CoV-2 (MOI of 1) or post-treatment with transfectant alone
1095 or in combination with 10 ng/μL of Poly(I:C) (normalized fold change over mock-infected, n=3
1096 independent experiments, ratio-paired t test, line at mean ± SEM). (**B**) RT-qPCR quantification of IFNβ,
1097 IFNλ1 and IFNλ2/3 transcripts induction in A549-ACE2 cells, 24 hours post infection at an MOI of 1
1098 with SARS-CoV-2 or Measles virus expressing GFP (MeV) or post treatment with transfectant alone or
1099 in combination with 10 ng/μL of Poly(I:C) (normalized fold change over mock-infected, n=3
1100 independent experiments, line at mean ± SEM).

1101 **Figure S5.** (**A**) Visualization of read coverage (tag/nucleotide) from polyA+ RNA-seq and ChIP-seq
1102 (IP – Input) at NFKB1, CXCL8, and IL32 loci. RNA-seq and ChIP-seq data were normalized
1103 independently, on ERCC reads for RNA-seq and on library size for ChIP-seq. (**B**) RT-qPCR
1104 quantification of NFKB1 and CXCL8 transcripts induction in A549-ACE2 cells, 24 hours post infection
1105 with SARS-CoV-2 (MOI of 1) (normalized fold change over mock-infected, n=3 independent
1106 experiments, ratio-paired t test, line at mean ± SEM).

1107 **Figure S6.** RT-qPCR quantification of three coding transcripts (**A**) and three lncRNAs (**B**) in A549-
1108 ACE2 cells, 3 hours post treatment with 10 ng/mL of TNFα or 24 hours post-SARS-CoV-2 infection
1109 (MOI of 1) (normalized fold change over mock-infected, n=3 independent experiments, ratio-paired t
1110 test, line at mean ± SEM).

1111

1112 **Supplementary tables**

1113

1114 Table S1. Differential expression analysis of mRNAs (infected S^+ vs mock, infected S^+ vs bystander,
1115 and bystander vs mock).

1116

1117 Table S2. Differential expression analysis of lncRNAs (infected S^+ vs mock, infected S^+ vs bystander,
1118 and bystander vs mock).

1119

1120 Table S3. Differential expression analysis of unannotated RNAs (infected S^+ vs mock, infected S^+ vs
1121 bystander, and bystander vs mock).
1122
1123 Table S4. Gene overlap between DE-seq from our 'sorted vs mock' samples and 'mixed vs mock'
1124 data re-analyzed from Blanco-Melo *et al.* 2020 (MOI of 0.2).
1125
1126 Table S5. This table shows known NF-κB target mRNAs, as well as predicted NF-κB target lncRNAs
1127 and unreferenced RNAs, among upregulated RNAs in S^+ vs mock cells.
1128

1129 Table S6. RT-qPCR primer sequences
1130
1131
1132
1133
1134

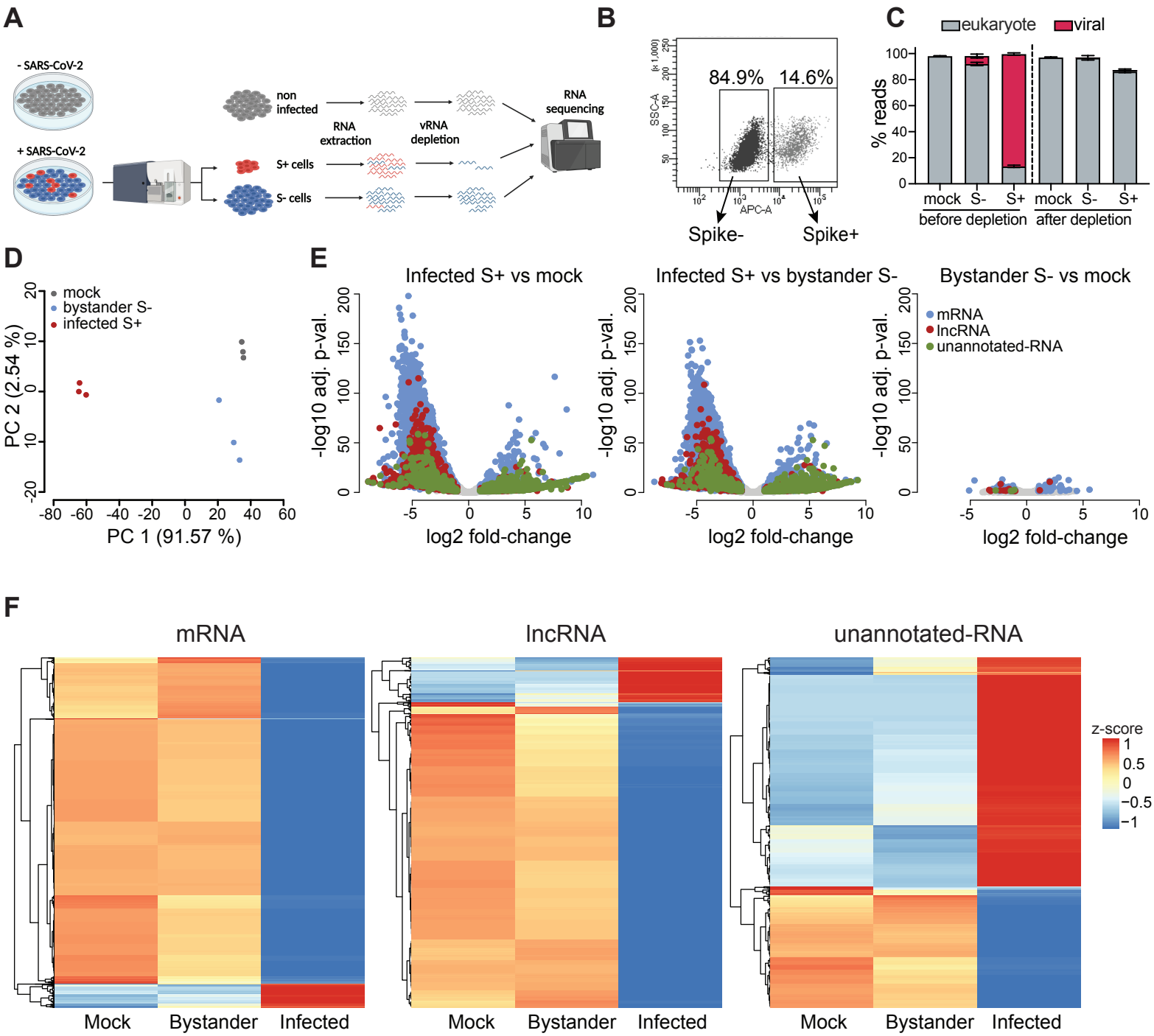
A
- SARS-CoV-2
+ SARS-CoV-2
non infected
S+ cells
S- cells
RNA extraction
vRNA depletion
RNA sequencing
B
84.9%
14.6%
SSC-A
APC-A
Spike-
Spike+
C
eukaryote
viral
% reads
mock
S-
S+
before depletion
after depletion
D
mock
bystander S-
infected S+
PC 2 (2.54 %)
PC 1 (91.57 %)
E
Infected S+ vs mock
Infected S+ vs bystander S-
Bystander S- vs mock
-log10 adj. p-val.
log2 fold-change
mRNA
lncRNA
unannotated-RNA
F
mRNA
lncRNA
unannotated-RNA
Mock
Bystander
Infected
z-score

Figure 1.

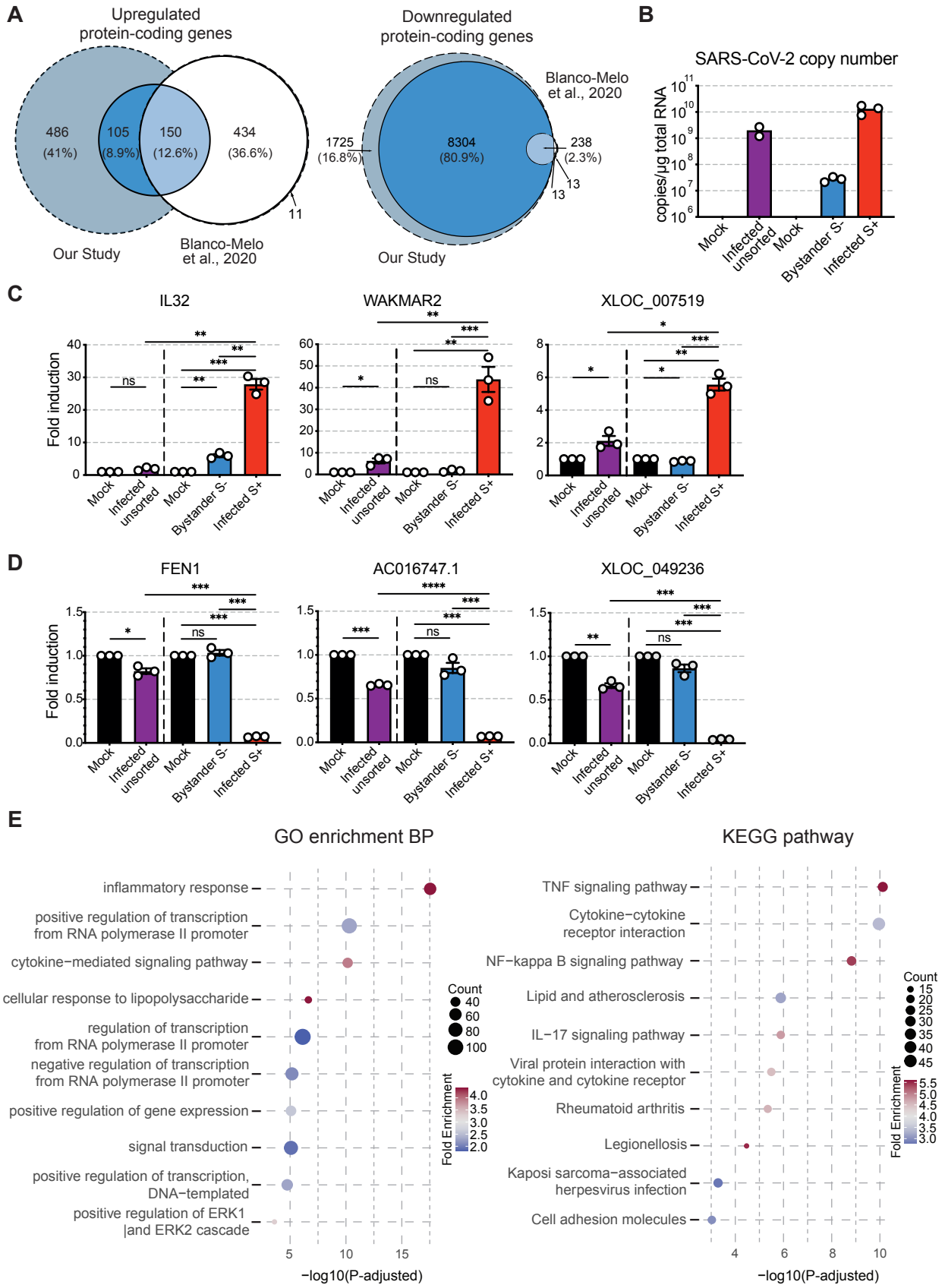
A
Upregulated protein-coding genes
486 (41%)
105 (8.9%)
150 (12.6%)
434 (36.6%)
11
Our Study
Blanco-Melo et al., 2020
Downregulated protein-coding genes
1725 (16.8%)
8304 (80.9%)
238 (2.3%)
13
13
Blanco-Melo et al., 2020
Our Study
B
SARS-CoV-2 copy number
copies/µg total RNA
Mock
Infected unsorted
Mock
Bystander S-
Infected S+
C
IL32
WAKMAR2
XLOC_007519
Fold induction
D
FEN1
AC016747.1
XLOC_049236
E
GO enrichment BP
inflammatory response
positive regulation of transcription from RNA polymerase II promoter
cytokine-mediated signaling pathway
cellular response to lipopolysaccharide
regulation of transcription from RNA polymerase II promoter
negative regulation of transcription from RNA polymerase II promoter
positive regulation of gene expression
signal transduction
positive regulation of transcription, DNA-templated
positive regulation of ERK1 |and ERK2 cascade
−log10(P-adjusted)
Count
Fold Enrichment
KEGG pathway
TNF signaling pathway
Cytokine-cytokine receptor interaction
NF-kappa B signaling pathway
Lipid and atherosclerosis
IL-17 signaling pathway
Viral protein interaction with cytokine and cytokine receptor
Rheumatoid arthritis
Legionellosis
Kaposi sarcoma-associated herpesvirus infection
Cell adhesion molecules
−log10(P-adjusted)
Count
Fold Enrichment

Figure 2.

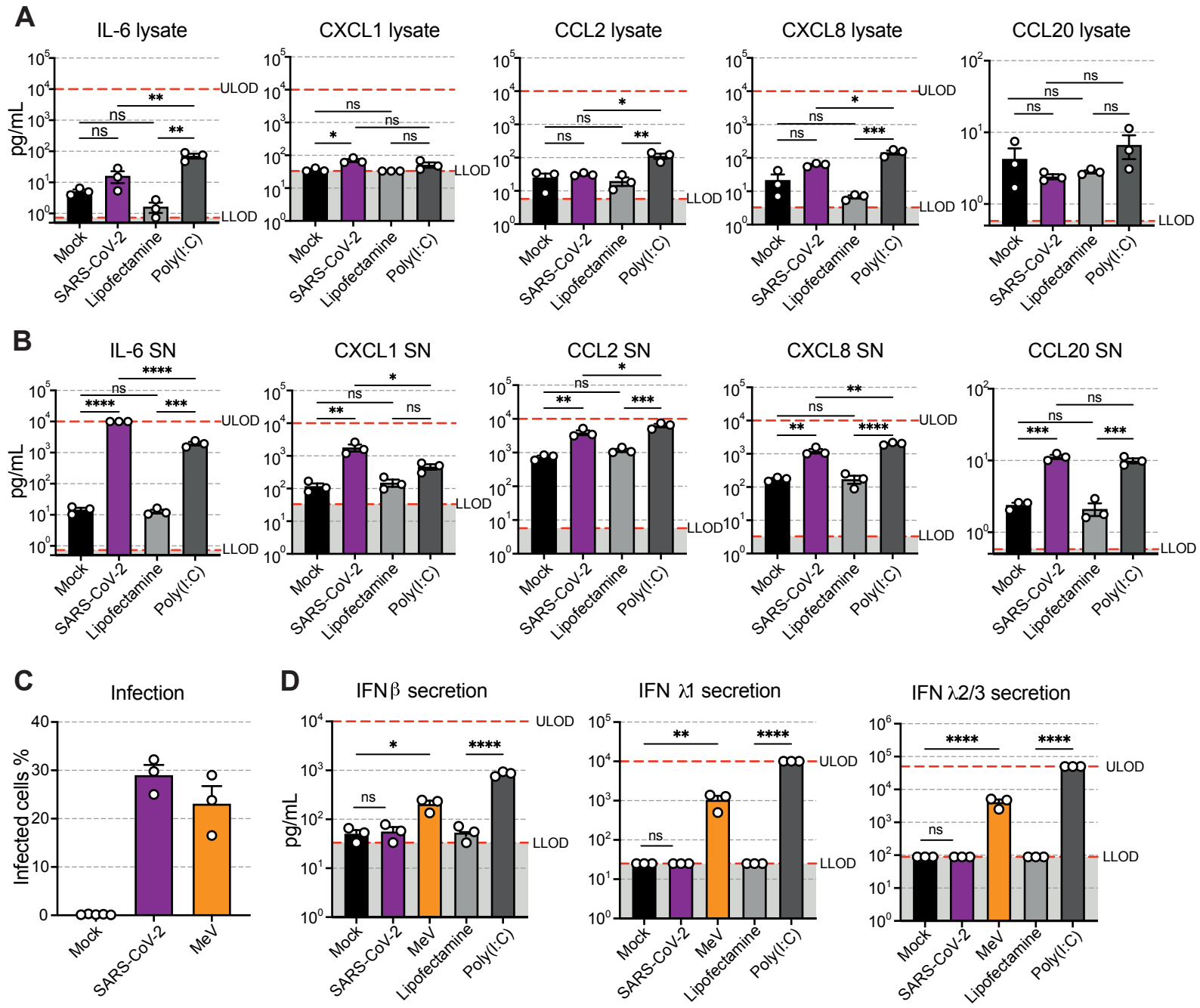
A
IL-6 lysate
CXCL1 lysate
CCL2 lysate
CXCL8 lysate
CCL20 lysate
pg/mL
ULOD
LLOD
Mock
SARS-CoV-2
Lipofectamine
Poly(I:C)
B
IL-6 SN
CXCL1 SN
CCL2 SN
CXCL8 SN
CCL20 SN
C
Infection
Infected cells %
MeV
D
IFNβ secretion
IFN λ1 secretion
IFN λ2/3 secretion

Figure 3.

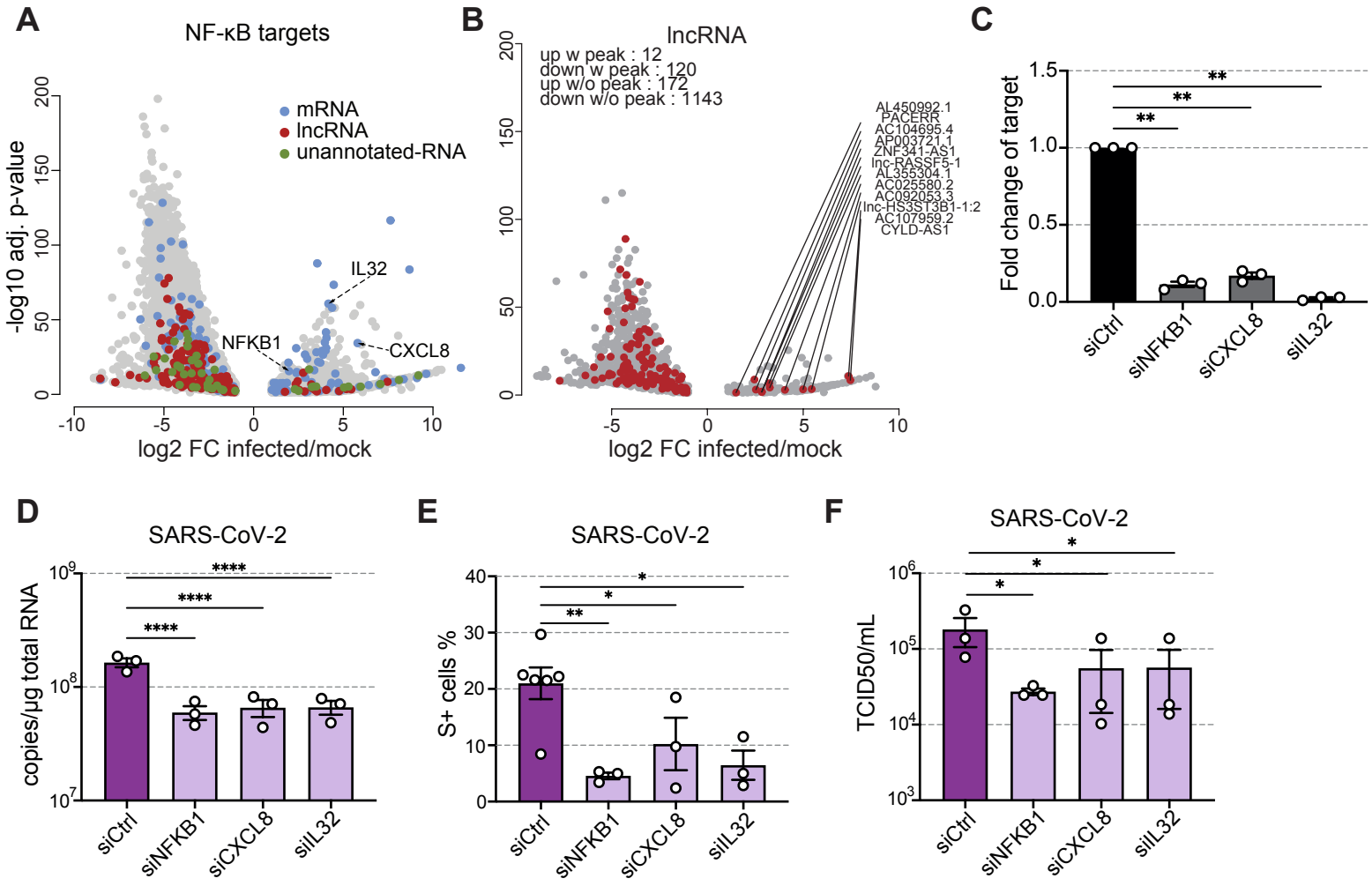
A
NF-κB targets
mRNA
lncRNA
unannotated-RNA
IL32
NFKB1
CXCL8
-log10 adj. p-value
log2 FC infected/mock
B
lncRNA
up w peak : 12
down w peak : 120
up w/o peak : 172
down w/o peak : 1143
AL450992.1
PACERR
AC104695.4
AP003721.1
ZNF341-AS1
lnc-RASSF5-1
AL355304.1
AC025580.2
AC092053.3
lnc-HS3ST3B1-1:2
AC107959.2
CYLD-AS1
log2 FC infected/mock
C
Fold change of target
siCtrl
siNFKB1
siCXCL8
siIL32
D
SARS-CoV-2
copies/µg total RNA
siCtrl
siNFKB1
siCXCL8
siIL32
E
SARS-CoV-2
S+ cells %
siCtrl
siNFKB1
siCXCL8
siIL32
F
SARS-CoV-2
TCID50/mL
siCtrl
siNFKB1
siCXCL8
siIL32

Figure 4.

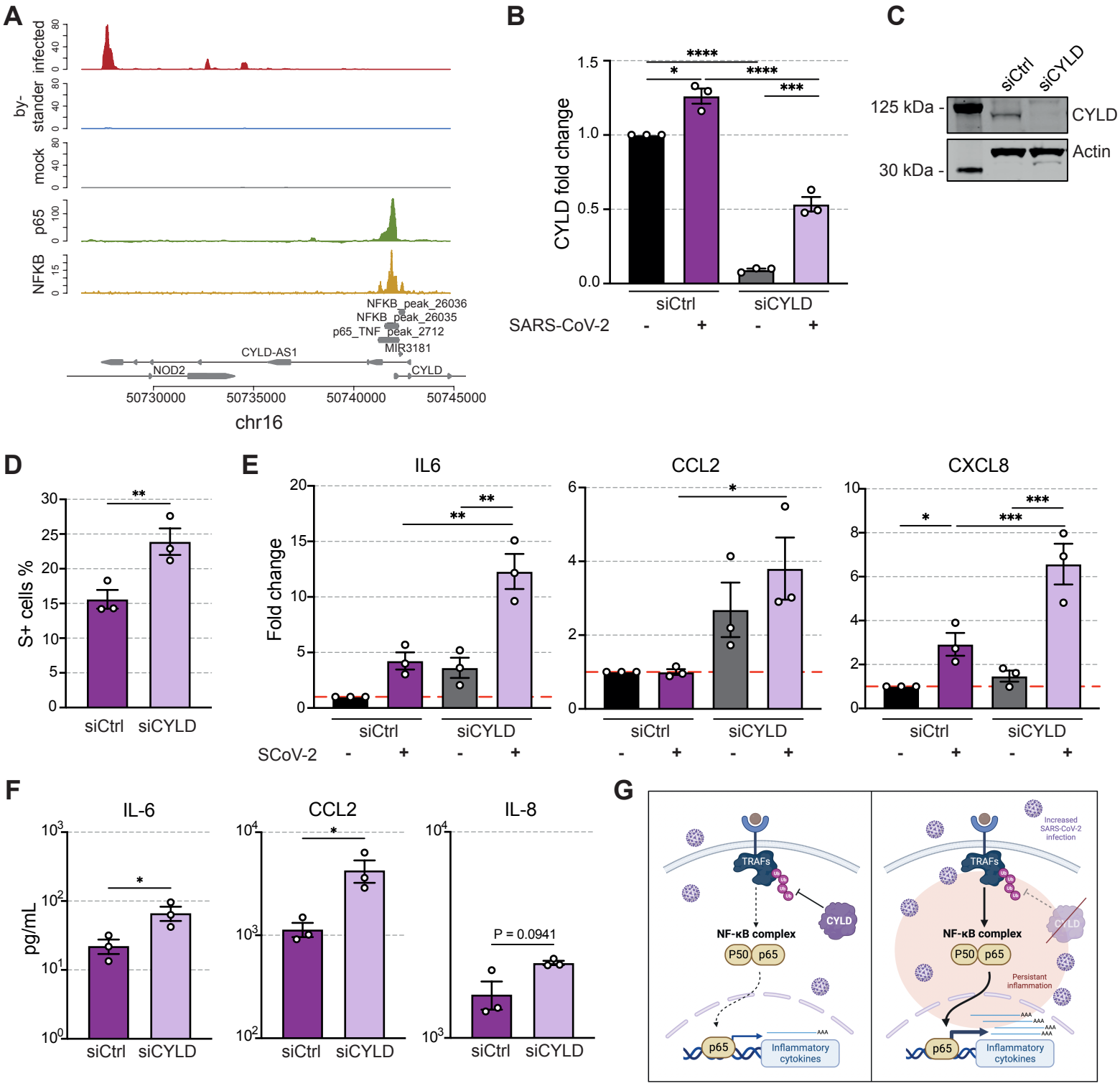
A
infected
by-stander
mock
p65
NFKB
NFKB_peak_26036
NFKB_peak_26035
p65_TNF_peak_2712
MIR3181
CYLD-AS1
NOD2
CYLD
50730000
50735000
50740000
50745000
chr16
B
CYLD fold change
siCtrl
siCYLD
SARS-CoV-2
C
siCtrl
siCYLD
125 kDa
30 kDa
CYLD
Actin
D
S+ cells %
siCtrl
siCYLD
E
IL6
CCL2
CXCL8
Fold change
SCoV-2
F
IL-6
CCL2
IL-8
pg/mL
P = 0.0941
G
TRAFs
CYLD
NF-κB complex
P50
p65
Inflammatory cytokines
Increased SARS-CoV-2 infection
Persistant inflammation

Figure 5.

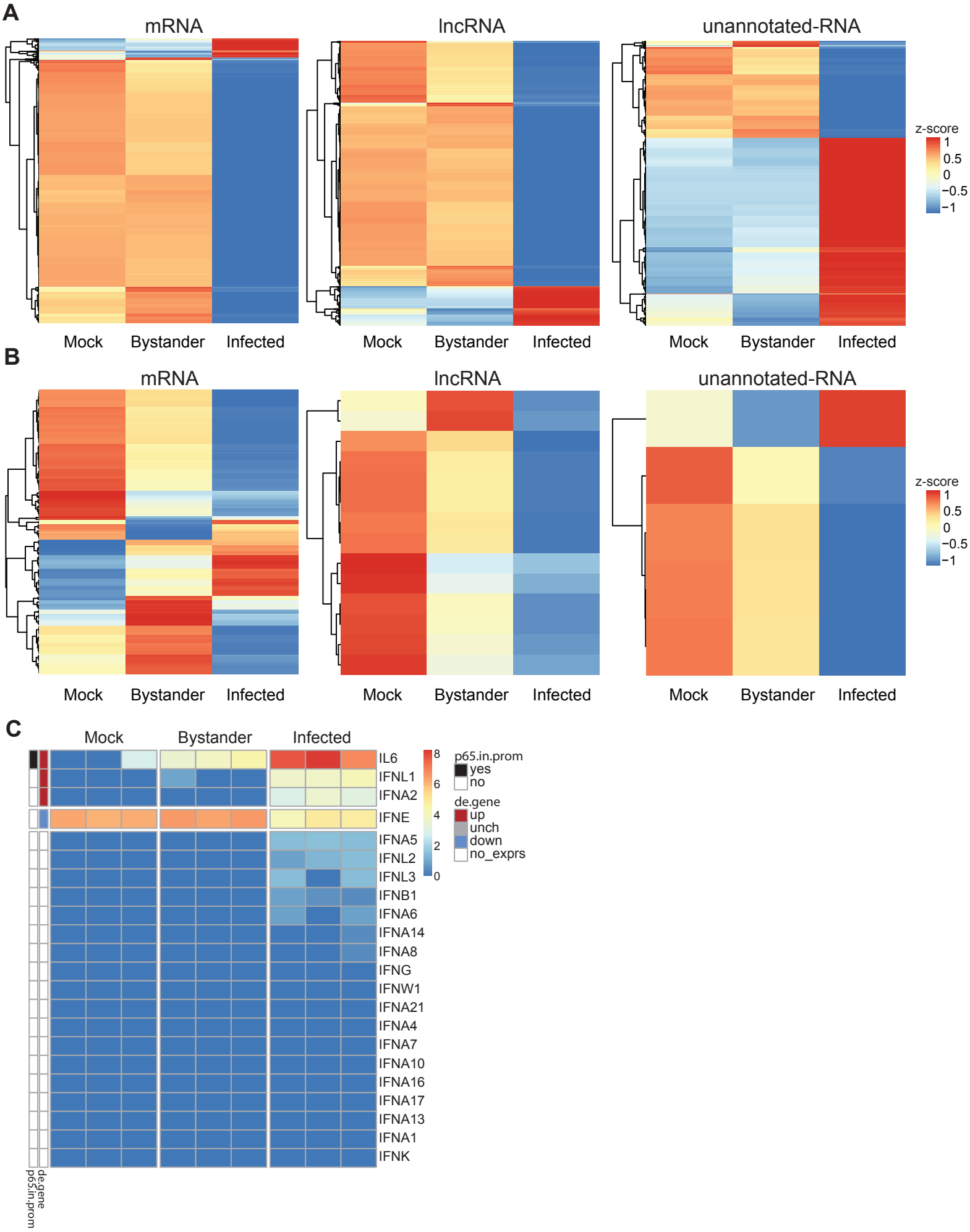
A
mRNA
lncRNA
unannotated-RNA
z-score
1
0.5
0
−0.5
−1
Mock
Bystander
Infected
B
mRNA
lncRNA
unannotated-RNA
z-score
1
0.5
0
−0.5
−1
Mock
Bystander
Infected
C
Mock
Bystander
Infected
IL6
IFNL1
IFNA2
IFNE
IFNA5
IFNL2
IFNL3
IFNB1
IFNA6
IFNA14
IFNA8
IFNG
IFNW1
IFNA21
IFNA4
IFNA7
IFNA10
IFNA16
IFNA17
IFNA13
IFNA1
IFNK
8
6
4
2
0
p65.in.prom
yes
no
de.gene
up
unch
down
no_exprs
de.gene
p65.in.prom

Figure S1.

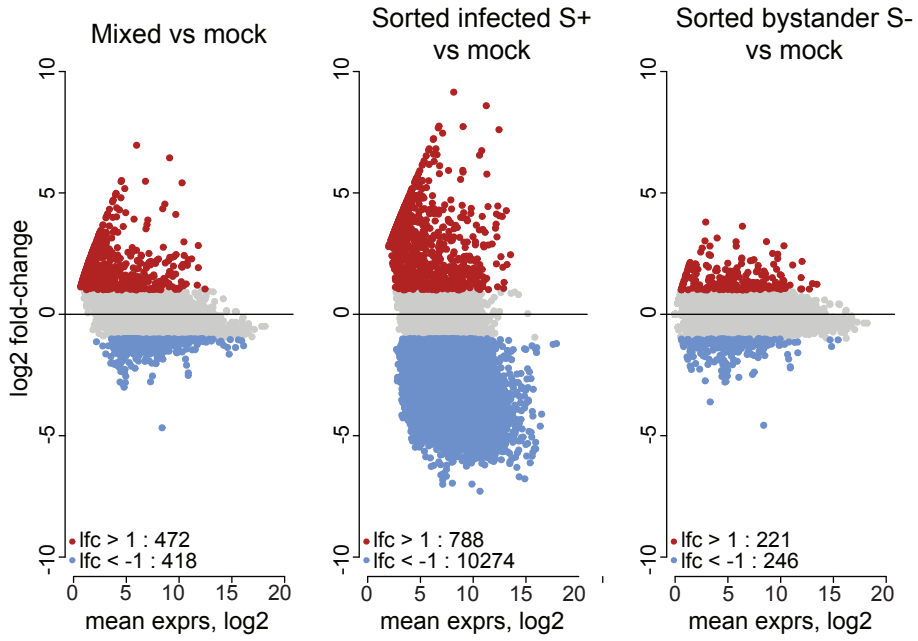
Mixed vs mock
Sorted infected S+ vs mock
Sorted bystander S- vs mock
log2 fold-change
mean exprs, log2
lfc > 1 : 472
lfc < -1 : 418
lfc > 1 : 788
lfc < -1 : 10274
lfc > 1 : 221
lfc < -1 : 246

Figure S2.

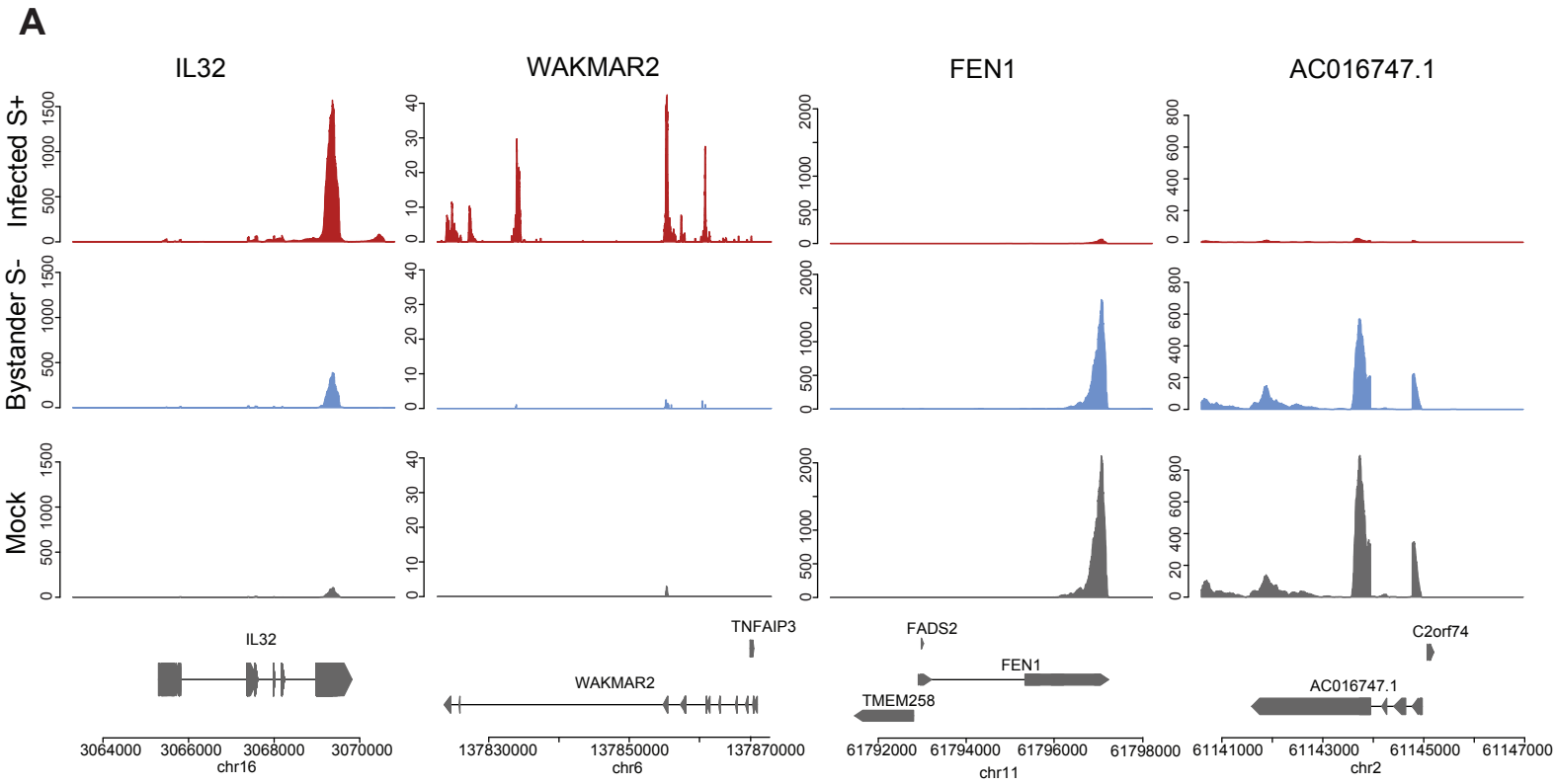
A
IL32
WAKMAR2
FEN1
AC016747.1
Infected S+
Bystander S-
Mock
IL32
TNFAIP3
WAKMAR2
FADS2
FEN1
TMEM258
C2orf74
AC016747.1
3064000 3066000 3068000 3070000
chr16
137830000 137850000 137870000
chr6
61792000 61794000 61796000 61798000
chr11
61141000 61143000 61145000 61147000
chr2

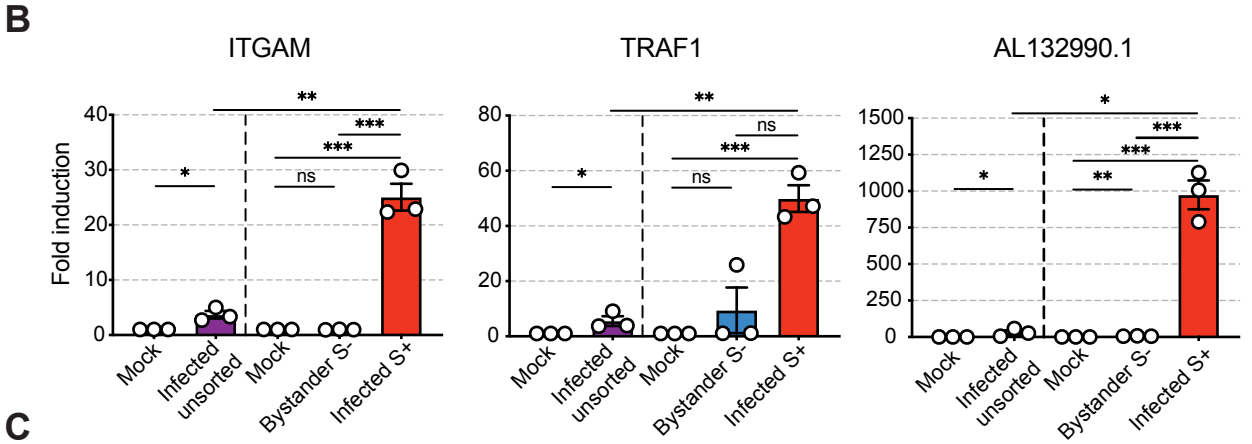
B
ITGAM
TRAF1
AL132990.1
Fold induction
Mock
Infected unsorted
Bystander S-
Infected S+

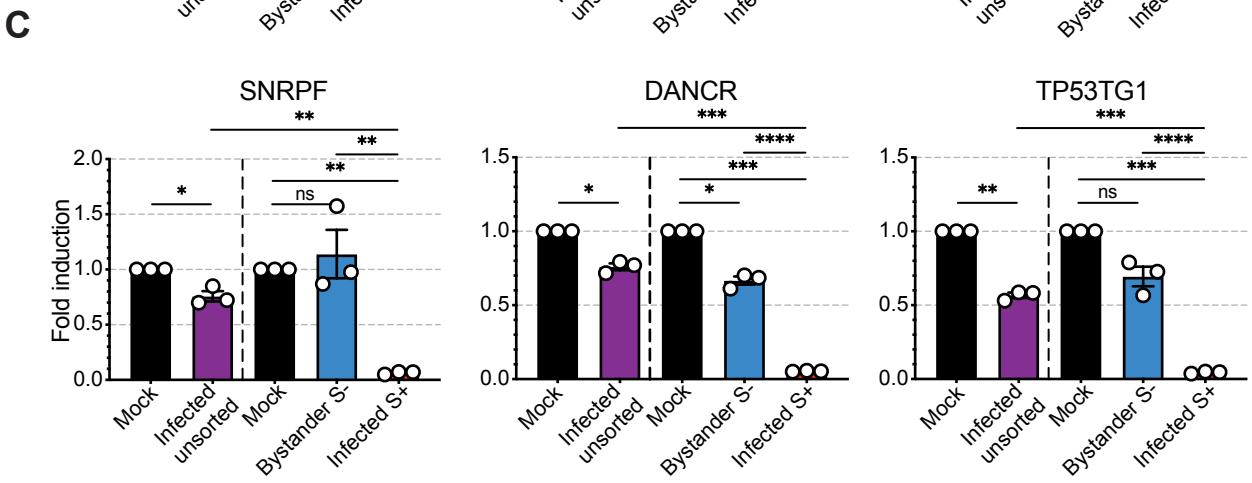
C
SNRPF
DANCR
TP53TG1
Fold induction
Mock
Infected unsorted
Bystander S-
Infected S+

Figure S3.

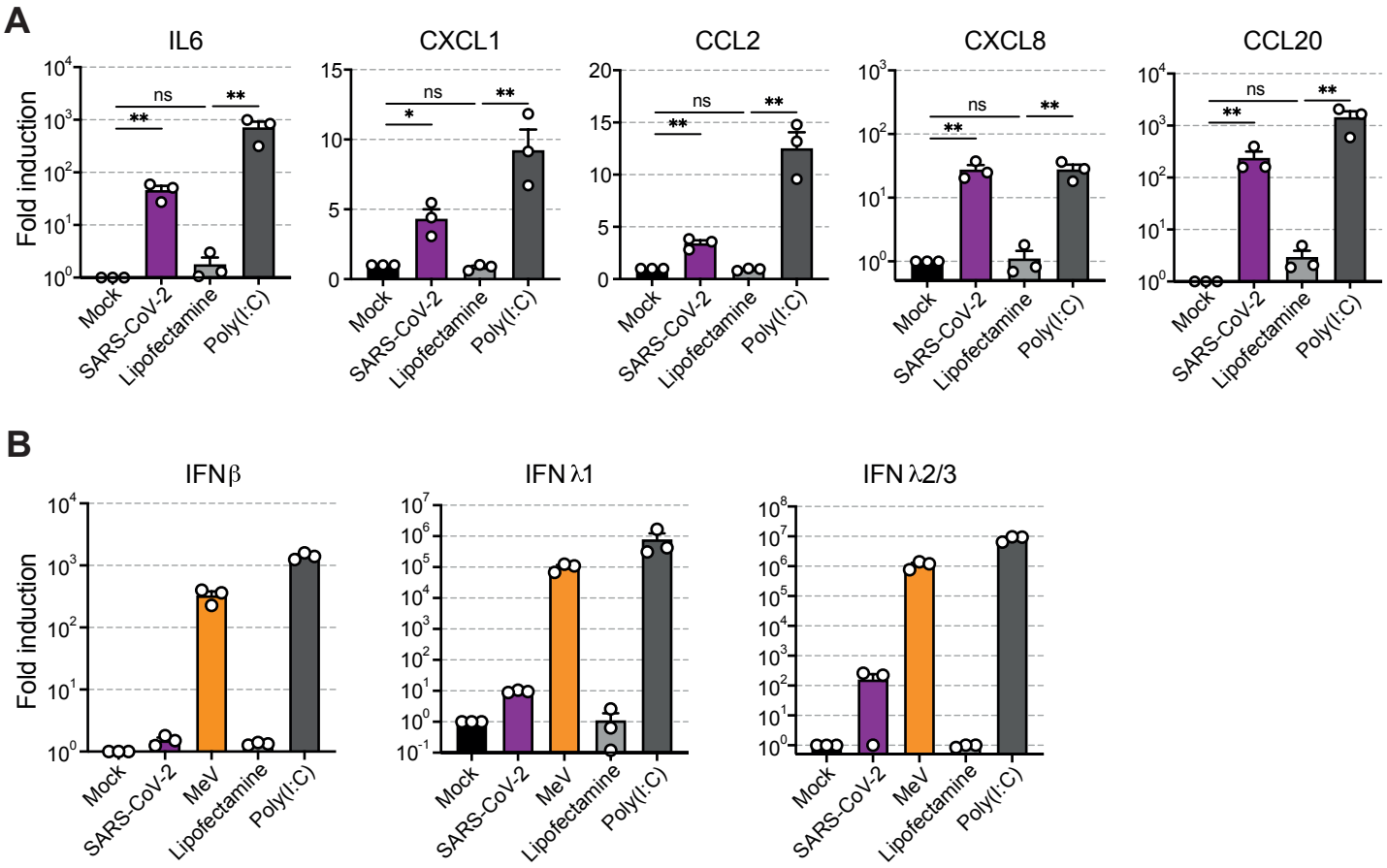
A
IL6
CXCL1
CCL2
CXCL8
CCL20
Fold induction
ns
**
*
Mock
SARS-CoV-2
Lipofectamine
Poly(I:C)
B
IFNβ
IFNλ1
IFNλ2/3
MeV

Figure S4.

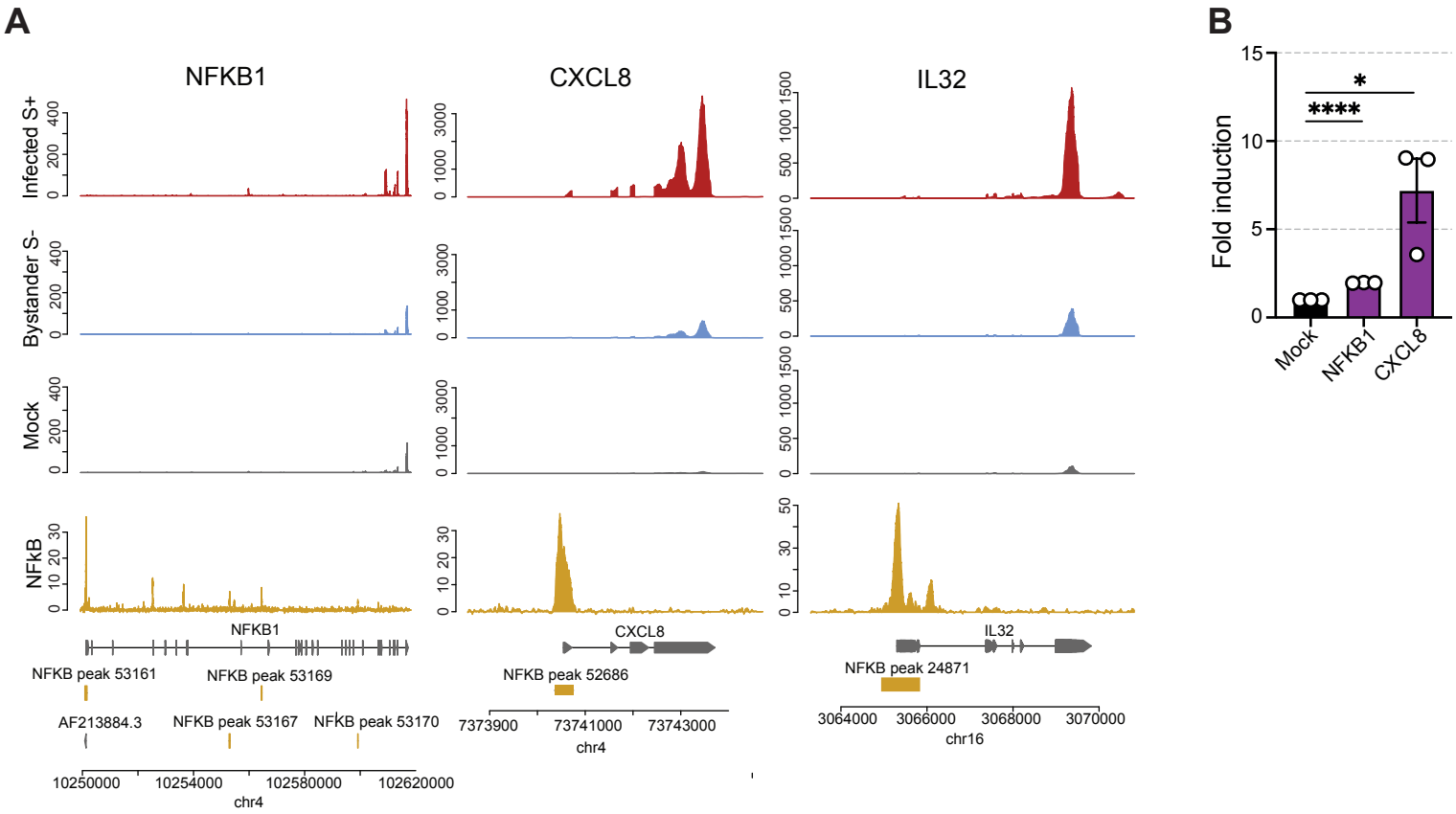
A
NFKB1
CXCL8
IL32
Infected S+
Bystander S-
Mock
NFkB
NFKB1
NFKB peak 53161
NFKB peak 53169
AF213884.3
NFKB peak 53167
NFKB peak 53170
10250000
10254000
102580000
102620000
chr4
CXCL8
NFKB peak 52686
7373900
73741000
73743000
chr4
IL32
NFKB peak 24871
3064000
3066000
3068000
3070000
chr16
B
Fold induction
Mock
NFKB1
CXCL8
*
****

Figure S5.

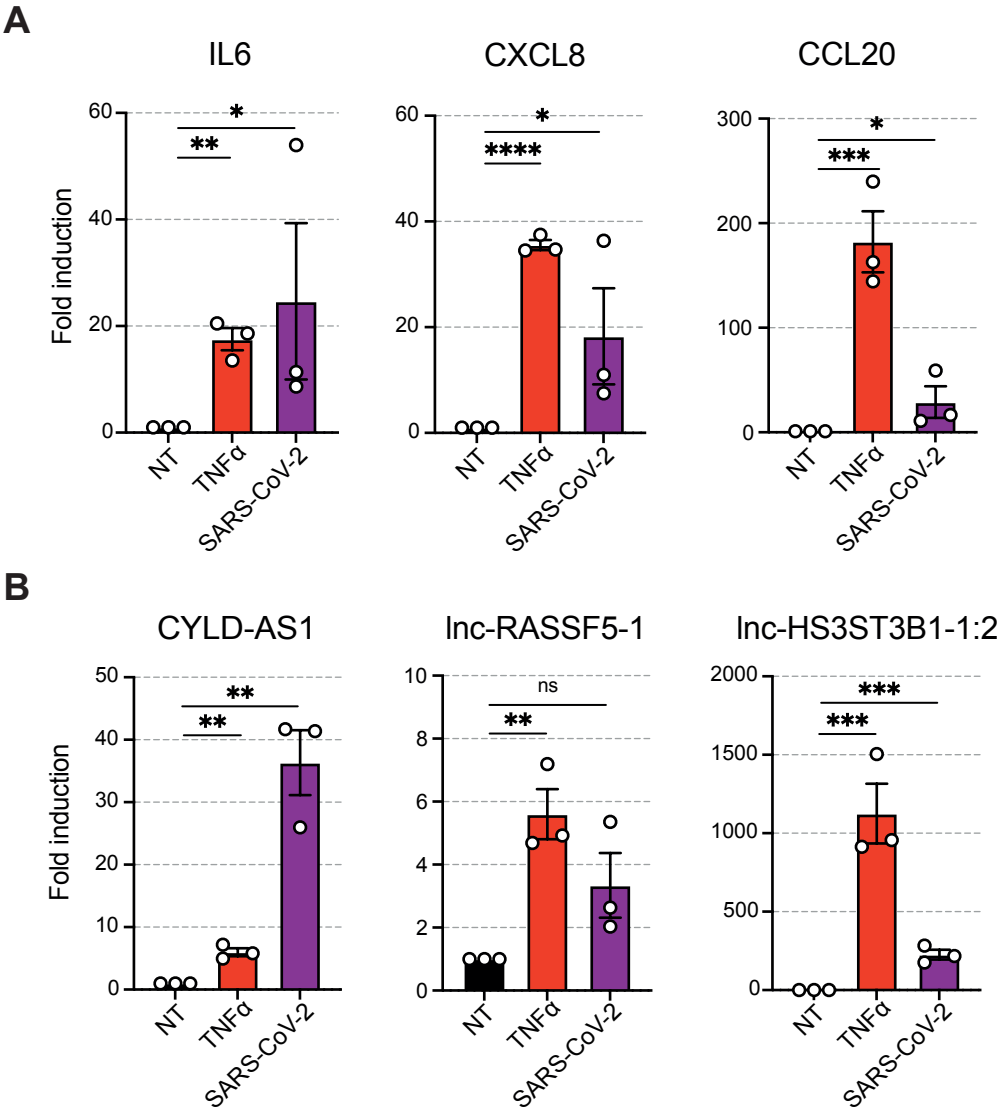
A
IL6
CXCL8
CCL20
Fold induction
NT
TNFα
SARS-CoV-2
B
CYLD-AS1
lnc-RASSF5-1
lnc-HS3ST3B1-1:2
ns

Figure S6.